JGR Atmospheres

RESEARCH ARTICLE
10.1029/2024JD041769

Updraft Width Modulates Ambient Atmospheric Controls on Convective Cloud Depth

A. C. Varble[1], Z. Feng[1], J. N. Marquis[1], Z. Zhang[2,3], A. Geiss[1], J. C. Hardin[1], and E. Jo[1]

[1]Atmospheric, Climate, and Earth Sciences Division, Pacific Northwest National Laboratory, Richland, WA, USA, [2]Department of Atmospheric Sciences, University of Utah, Salt Lake City, UT, USA, [3]Now at Department of Physics, University of Oxford, Oxford, UK

Manuscript Authored by Battelle Memorial Institute under contract number DE-AC05-76RL01830 with the US Department of Energy. The US Government retains and the publisher, by accepting this article for publication, acknowledges that the US Government retains a non-exclusive, paid-up, irrevocable, world-wide license to publish or reproduce the published form of this manuscript, or allow others to do so for US Government purposes. The Department of Energy will provide public access to these results of federally sponsored research in accordance with the DOE Public Access plan (http://energy.gov/downloads/doe-public-access-plan).

Key Points:

- Wide convective cell depth responds most to available instability, while narrow cell depth responds most to midlevel relative humidity
- Entrainment-driven reduction of buoyancy decreases as cell width increases, causing disparate narrow and wide cell depth responses
- A convection-permitting simulation with 3-km horizontal grid spacing generally reproduces observed relationships

Supporting Information:

Supporting Information may be found in the online version of this article.

Correspondence to:

A. C. Varble,
adam.varble@pnnl.gov

Citation:

Varble, A. C., Feng, Z., Marquis, J. N., Zhang, Z., Geiss, A., Hardin, J. C., & Jo, E. (2024). Updraft width modulates ambient atmospheric controls on convective cloud depth. *Journal of Geophysical Research: Atmospheres*, *129*, e2024JD041769. https://doi.org/10.1029/2024JD041769

Abstract The depth of convective clouds affects vertical transport of atmospheric constituents, influencing downstream weather and climate. Atmospheric controls on the maximum depth reached by moist convection are investigated with radar-tracked convective cells tagged with sounding-derived atmospheric parameters from a field campaign in central Argentina. Regression analyses show that narrow (<12-km diameter) and wide (>16-km diameter) cell depths respond to disparate factors, where cell areas are defined using composite reflectivity signatures. Undiluted lifted parcel indices including convective available potential energy (CAPE) and level of neutral buoyancy (LNB) are top predictors of wide cell maximum depth while mid-tropospheric relative humidity is the top predictor of narrow cell maximum depth. Because narrow cells are more numerous than wide cells, the overall outcome of the full cell population does not strongly correlate with CAPE and LNB conditions. Tracked cells and atmospheric conditions in a simulation with 3-km grid spacing covering the field campaign produce similar results to those observed. Narrow cells that are relatively deep have a cooler and moister mid-troposphere with weaker free tropospheric subsidence, while relatively deep wide cells have much warmer and moister lower tropospheric conditions. These atmospheric differences are present 1 hr before cell initiation at both a fixed observing site and variable cell initiation locations. Simulated narrow cell maximum equivalent potential temperature decreases with height at a rate similar to the ambient vertical gradient, causing these cells to fall short of their LNB and supporting the view that entrainment-driven dilution is a dominant control on their depth.

Plain Language Summary The depth that storms reach impacts where the heat, moisture, momentum, aerosols, and trace gases that they are transporting are deposited, but this depth is difficult to predict because most storms fall short of their theoretically maximum possible depth. The reason for this shortfall is that most storms are narrow, such that they are effectively diminished by mixing with surrounding drier air as the storm deepens. Thus, a dominant control on the depth of these clouds is the humidity of this surrounding air. However, wide storms are less vulnerable to destructive mixing with dry air. As a result, they more consistently reach depths that are well predicted by theory. These conclusions were reached via analysis of over a thousand storms over several months using field experiment measurements and a computer simulation.

1. Introduction

Moist convection is a primary pathway for vertical transport of atmospheric heat, moisture, momentum, aerosols, and trace gases (e.g., Barth et al., 2015; Dickerson et al., 1987; Houze, 1973; LeMone, 1983; Moncrieff, 1992; Riehl & Malkus, 1958). The heights and temperatures at which these constituents are detrained from convection into the atmosphere are strongly modulated by the depth reached by convective clouds. These detrainment heights further influence horizontal transport and lifetimes of such properties because of changes in winds and stability with height.

The depth of moist convection can be estimated given an atmospheric thermodynamic profile by lifting a saturated, buoyant air parcel until it becomes negatively buoyant at the level of neutral buoyancy (LNB; also known as the equilibrium level). Convective clouds reaching or overshooting the LNB in situations where the LNB is comparable to or higher than the tropopause is an important mechanism for mixing between the troposphere and stratosphere (e.g., Dessler & Sherwood, 2004; Pan et al., 2014; Wang, 2003). Assumptions are required to estimate the LNB from a sounding. First, a parcel starting level or mixed layer needs to be chosen for lifting. Common choices are the surface parcel, the most unstable parcel starting height, or a layer with adiabatically

Received 14 JUN 2024
Accepted 17 NOV 2024

Author Contributions:
Conceptualization: A. C. Varble, Z. Feng, J. N. Marquis
Data curation: A. C. Varble, Z. Zhang, J. C. Hardin
Formal analysis: A. C. Varble
Funding acquisition: A. C. Varble
Investigation: A. C. Varble
Methodology: A. C. Varble, Z. Feng, J. N. Marquis, Z. Zhang, A. Geiss, E. Jo
Project administration: A. C. Varble
Software: A. C. Varble, Z. Feng, J. N. Marquis, Z. Zhang, J. C. Hardin
Validation: A. C. Varble, A. Geiss
Visualization: A. C. Varble, J. N. Marquis
Writing – original draft: A. C. Varble
Writing – review & editing: A. C. Varble, Z. Feng, J. N. Marquis, Z. Zhang, A. Geiss, E. Jo

mixed properties. Irreversible pseudoadiabatic ascent assumes all condensates immediately leaves the parcel. This leads to a different LNB height than assuming reversible ascent in which all condensates are carried with the parcel. Inclusion of freezing further alters the LNB. Cloud-scale processes occurring during realistic ascent alter updraft buoyancy. For example, the parcel's buoyancy and LNB are reduced via mixing with air from the surrounding environment, while both are increased by the latent heat of fusion as the condensate freezes. Such effects, which depend on updraft width (e.g., Morrison, 2017; Peters et al., 2020), condensate mass (e.g., Igel & van den Heever, 2021), and freezing (e.g., Peters et al., 2023) properties, are often neglected in lifted parcel convection metrics because they cannot be solely determined from a sounding. Thus, while the LNB is a good first guess of the maximum depth that convective clouds will reach, it can be highly sensitive to assumptions made to approximate parcel ascent.

Regardless of the choices for LNB definition, many convective clouds stop short of reaching it, producing a level of maximum detrainment lower than the LNB height (Mullendore et al., 2013; Takahashi & Luo, 2012; Wang, Giangrande, et al., 2020; Wang, Jensen, et al., 2020). A primary cause of clouds falling short of reaching the LNB is mixing of updraft air with surrounding cooler and drier air that lowers buoyancy. Idealized modeling studies have shown that the depth reached by convective clouds decreases as updraft width decreases (e.g., Grabowski et al., 2006; Khairoutdinov & Randall, 2006; Kuang & Bretherton, 2006; Morrison, 2017; Morrison et al., 2020, 2022; Nelson et al., 2022; Peters et al., 2020; Powell, 2024; Rousseau-Rizzi et al., 2017; Schlemmer & Hohenegger, 2014) and free tropospheric relative humidity (RH) decreases (e.g., Chaboureau et al., 2004; Derbyshire et al., 2004; Hannah, 2017; Morrison, 2017; Morrison et al., 2020, 2022; Nelson et al., 2022; Peters et al., 2020; Rousseau-Rizzi et al., 2017) due to their regulation of entrainment-driven dilution. Observational studies have also shown this to be the case (e.g., Brown & Zhang, 1997; Marquis et al., 2021, 2023; Nelson et al., 2021; Takahashi et al., 2021; Takemi et al., 2004; Zhang & Klein, 2010). The ability for an updraft of a given width and ambient environment to continue rising further depends on the vertical distribution of CAPE because more positively buoyant parcels can withstand more dilution and condensate loading before becoming negatively buoyant (e.g., Giangrande et al., 2023; Houston & Niyogi, 2007; Lucas et al., 1994; Wu et al., 2009). Lastly, vertical wind shear may also modulate the magnitude and spatial distribution of entrainment (e.g., Zhao & Austin, 2005) with complex alteration of updraft dilution. However, shear effects on cloud deepening can be net positive or negative depending on updraft width, low-level updraft inflow, vertical pressure gradients, and condensate unloading (e.g., Kirshbaum & Straub, 2019; LeBel & Markowski, 2023; Markowski et al., 2006; Nelson et al., 2022; Peters et al., 2019, 2022a, 2022b; Tian et al., 2021).

Much of the understanding about convective deepening in relation to updraft width, entrainment, and ambient atmospheric conditions has been derived from modeling. This is partly due to the ability to set up models in ways that carefully control for atmospheric and cloud states. Such setups also allow for comparisons to theoretical solutions and have shown that moist convective updrafts can take the form of an isolated shedding thermal, a chain of thermals, or a plume depending on the width of the updraft and the ambient atmospheric state (Hernandez-Deckers & Sherwood, 2016; Kirshbaum, 2011; Morrison et al., 2020; Moser & Lasher-Trapp, 2017; Peters et al., 2020; Romps & Charn, 2015; Sherwood et al., 2013), which is supported by observed cases (e.g., Blyth et al., 1988; Blyth et al., 2005; Damiani et al., 2006). Such morphologies influence how ambient air is entrained into and interacts with the updraft. Simulations only form thermals if they are sufficiently resolved, which typically requires model grid spacing of hundreds of meters or less (e.g., Bryan et al., 2003; Bryan & Morrison, 2012; Lebo & Morrison, 2015). Under-resolved convective updrafts are biased wide (Prein et al., 2021; Tang & Kirshbaum, 2020; Varble et al., 2020; Wang, Giangrande, et al., 2020; Wang, Jensen, et al., 2020), which can lead to more plume-like behavior with biased perturbation pressure, buoyancy, and entrainment-driven dilution (Varble et al., 2014). Unfortunately, three-dimensional simulations with O(100-m) horizontal grid spacing covering domains that are hundreds of kilometers across are computationally expensive and thus primarily limited to case studies. Though valuable, case studies require context from the vast spectrum of known convective cloud properties and atmospheric conditions. Thus, kilometer-scale simulations in which convective clouds are not parameterized and also not fully resolved remain essential because of their ability to run over large domains and long periods of time. Such simulations are currently central to regional weather prediction (Benjamin et al., 2018) and soon will be central to climate prediction (Stevens et al., 2019).

Observations are required to assess how well models represent convective deepening processes such that modeling studies can be properly interpreted, but several factors have limited observational results. First, the real world produces a spectrum of cloud depths arising from variability in updraft width and near-cloud atmospheric

conditions due to factors such as mesoscale heterogeneity, complex terrain, and interactions between neighboring clouds (e.g., Liu et al., 2023; Marquis et al., 2021, 2023; Nelson et al., 2021) that are neither accounted for in idealized simulations nor adequately sampled by routine measurements. Second, individual convective cells need to be tracked in space and time, typically by radar or satellite methods with strengths and limitations in their ability to accurately retrieve the convective cell life cycle properties. Lastly, updraft width, speed, buoyancy, and microphysical properties are rarely observed with sufficient accuracy and resolution for studying cloud growth processes. Exacerbating these issues, updrafts do not share a singular definition across observational studies due to retrievals with variable resolution and uncertainty. Contiguous vertical wind speed objects in space or time using a threshold minimum vertical wind speed of 0–2 m s^{-1} are a common definition in the limited situations in which vertical wind speed retrievals are possible (e.g., Varble et al., 2014; Wang, Giangrande, et al., 2020; Wang, Jensen, et al., 2020). Thus, even though models contain biases, they are often required to connect processes and properties in ways that inform accurate interpretation of observations.

In this study, we use both a regional convection-permitting simulation and observations collected during the 6.5-month-long Cloud, Aerosol, and Complex Terrain Interactions (CACTI) field campaign (Varble et al., 2021) to track convective cell properties across a diversity of meteorological conditions. The objectives of this study are twofold. One objective is to determine whether updraft width across many cases and variable conditions regulates the response of convective cloud depth to atmospheric conditions as suggested in past idealized modeling studies and observational cases. Our overarching hypothesis is that relatively narrow cells have narrow updrafts with maximum depths more regulated by entrainment-driven dilution than their undiluted potential. In contrast, relatively wide cells have wide updrafts that reach depths well predicted by undiluted CAPE and LNB metrics. The other objective is to assess the ability of a regional convection-permitting simulation with 3-km horizontal grid spacing to reproduce observed relationships between cell width, depth, and atmospheric conditions. Section 2 describes observational and modeling data sets used, while Section 3 describes the study methodology. Results are presented in Section 4 with conclusions in Section 5.

2. Data Sets

2.1. Observations

Measurements of convective cell and atmospheric properties are obtained from the U.S. Department of Energy Atmospheric Radiation Measurement (ARM) CACTI field campaign, which occurred between October 2018 and April 2019 over the Sierras de Córdoba range of central Argentina (Varble et al., 2021). This region supports frequent initiation and growth of deep convection (Mulholland et al., 2018, 2020; Rasmussen & Houze, 2011, 2016; Singh et al., 2022) across a wide variety of atmospheric conditions (Schumacher et al., 2021). Data were collected in conjunction with the National Science Foundation led Remote sensing of Electrification, Lightning, and Mesoscale/microscale Processes with Adaptive Ground Observations (RELAMPAGO) field campaign (Nesbitt et al., 2021). Several studies have already leveraged RELAMPAGO-CACTI data sets to investigate processes including mechanical and thermal orographic flow effects on cumulus convection (Lareau et al., 2024), aerosol and turbulence effects on warm cloud precipitation (Borque et al., 2022), deep convection initiation (Marquis et al., 2021, 2023; Nelson et al., 2021, 2022), convective cloud microphysics and lightning (Casanovas et al., 2021; Elkins & Hence, 2024; Lang et al., 2020; Medina, Carey, Bitzer, et al., 2022; Medina, Carey, Deierling, & Lang, 2022; Rivelli Zea et al., 2021; Rocque et al., 2024), deep convective upscale growth and evolution (Feng et al., 2022; Lombardo & Kumjian, 2022; Trapp et al., 2020; Zhang et al., 2021, 2024), and aerosol effects on convective clouds (Medina, Carey, Bitzer, et al., 2022; Medina, Carey, Deierling, & Lang, 2022; Ross & Lasher-Trapp, 2024; Veals et al., 2022).

Radar reflectivity from the C-band Scanning ARM Precipitation Radar (C-SAPR2) is used to define and track observed convective cells and their properties (see Figure 1 and Section 3). C-SAPR2 performed a repeating 15-min scan sequence that included a plan position indicator (PPI) scan volume with elevation angles between 0.5° and 33° (Hardin et al., 2018). PPI data are missing from late December through January 20, in mid-February, and after March 2, resulting in about 3.5 months of cell tracks used here. The radar was calibrated with on-site measurements and comparisons with other radars (Hardin, Hunzinger, et al., 2020) with further data processing performed with Taranis software (Hardin, Bharadwaj, et al., 2020) (see Feng et al. (2022) and Hardin et al. (2024) for more details). Radial radar data are Cartesian gridded with Cressman weighting and a range-dependent linearly increasing radius of influence using default settings in the Python ARM Radar Toolkit

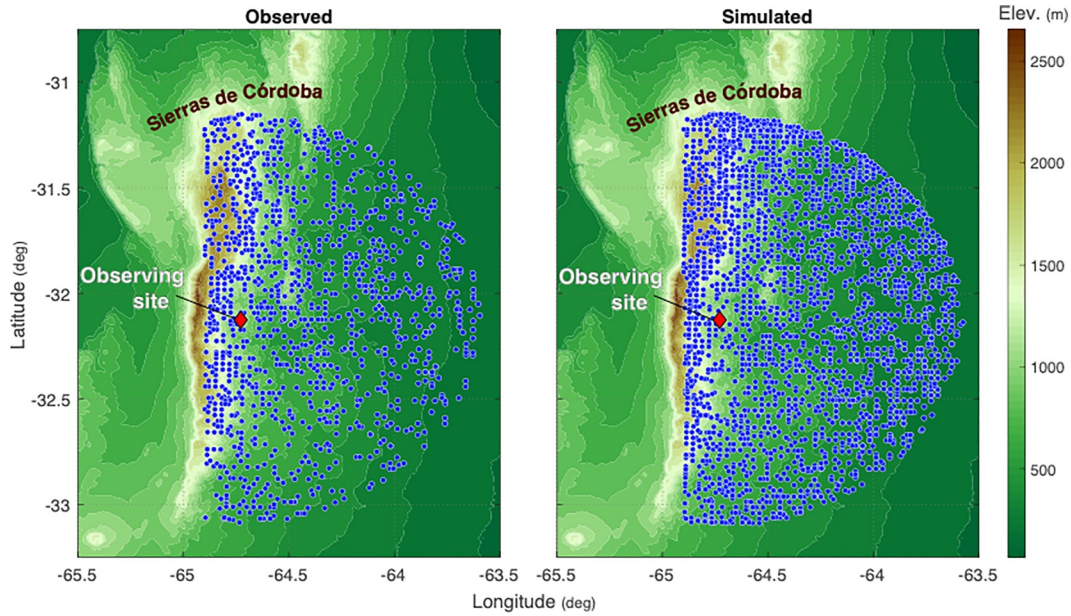

Figure 1. A topographic map showing the observing (CSAPR2 and radiosonde) site (red diamond) and the cell initiation locations (blue dots) for observations (left) and WRF (right).

(Helmus & Collis, 2016) with 500-m horizontal and vertical grid spacing out to a horizontal range of 110 km and vertical depth of 20 km above the radar altitude (1,141 m). Radar reflectivity is then averaged in linear units to 3-km horizontal grid spacing to match the grid spacing of model output described in Section 2.2.

Satellite Cloud and Radiation Property System (SatCORPS) Geostationary Operational Environmental Satellite 16 (GOES-16) cloud products (Minnis et al., 2021; Smith & Thieman, 2019; Trepte et al., 2019; Yost et al., 2021) are used to quantify top-of-atmosphere infrared brightness temperature (TOA IR T_b). These retrievals have a resolution of approximately 2 km and 15 min. They are parallax corrected and converted back to a regular grid using a nearest neighbor approach in scikit-learn (Pedregosa et al., 2011) and choosing values associated with the coldest cloud top pixel for overlapping irregular points (Varble, Thieman, et al., 2024). They are then colocated with the radar data using the nearest neighbor method in xESMF (Zhuang, 2020).

Radiosondes were launched at the observing site (Figure 1) between 12:00 (09:00 local time) and 00:00 (21:00 local time) UTC with 3-hourly frequency on days in which deep convection was forecasted and 4-hourly frequency on other days. These soundings were inputted to the ARM Interpolated Sounding product (Fairless & Giangrande, 2018; Fairless et al., 2021) that linearly interpolates atmospheric state variables to a 1-min resolution at 332 constant height levels using microwave radiometer retrieved total column water vapor (TCWV; Turner et al., 2007; Gaustad et al., 2011). Computed atmospheric parameters follow Nelson et al. (2021) and Marquis et al. (2023) with a subset chosen based on their potential to impact convective updraft width, depth, and intensity (Table 1). These measurements are matched in time with the 15-min radar and satellite data sets. Analyzed pseudoadiabatic most unstable (MU) lifted parcel metrics include convective available potential energy (MUCAPE), convective inhibition (MUCIN), MU-lifted condensation level (LCL) height and temperature, MU level of free convection (LFC), and MU level of neutral buoyancy (LNB). Reversible ascent metrics not including fusion were also computed, but pseudoadiabatic parameters are used because they generally exhibited slightly higher correlation coefficients with cell depths. The MU parcel starting height and the water vapor mixing ratio were also assessed but removed from analyses because of high correlation with MU LCL height and temperature. Bulk wind difference (BWD) in the 0–3 and 0–6 km AGL layers are used as metrics of vertical wind shear. TCWV and 5-km ASL relative humidity (RH) are computed to characterize ambient moisture. RH at other height levels were also tested but exhibited weaker correlations with cell depth. Lastly, the CAPE, mean RH, and BWD in the active cloud bearing layer (ACBL) are assessed where the ACBL is the 1.5-km deep layer with the MULFC height as its lower bound, following Lock and Houston (2014). This is the layer where lifted MU parcels are first positively buoyant and potentially particularly susceptible to entrainment-driven buoyancy dilution.

Table 1
Convective Cell and Atmospheric Variables Used in This Study

Convective cell properties	
Max Diameter	Cell lifetime-maximum diameter
Max 10-dBZ ETH	Cell lifetime-maximum 10-dBZ echo top height
Min TOA IR T_b	Cell lifetime-minimum top-of-atmosphere infrared brightness temperature
Max Reflectivity	Cell lifetime-maximum radar reflectivity
Lifetime	Cell lifetime
Sounding-derived pseudoadiabatic most unstable lifted parcel parameters	
MU LNB	Level of neutral buoyancy
MUCAPE	Convective available potential energy
MUCIN	Convective inhibition
MU LCL Height	Lifted condensation height level above ground
MU LFC Height	Level of free convection height above ground
MU LCL Temp	Lifted condensation height level temperature
ACBL CAPE	Active cloud bearing layer convective available potential energy
ACBL RH	Active cloud bearing layer relative humidity
ACBL BWD	Active cloud bearing layer bulk wind difference
Additional sounding-derived atmospheric parameters	
TCWV	Total column water vapor
5 km RH	5 km above sea level relative humidity
0–3 km BWD	0–3 km above ground level bulk wind difference
0–6 km BWD	0–6 km above ground level bulk wind difference

2.2. Model Setup and Output

The Weather Research and Forecasting (WRF) model V4.1.1 (Skamarock et al., 2019) was used to perform a 6.5-month long simulation covering the entire CACTI field campaign over a 1,800 km × 1,500 km region (see Zhang et al. (2021) and Sasaki et al. (2024) for further details). The simulation uses 3-km horizontal grid spacing with 80 vertical levels that maintain 250 m or less vertical grid spacing below 5-km altitude to better resolve temperature inversions. Initial and boundary conditions are provided by the European Centre for Medium-Range Weather Forecasts Reanalysis v5 (ERA5; Hersbach et al., 2020) with no nudging applied. The Thompson aerosol-aware microphysics scheme (Thompson & Eidhammer, 2014) is used with aerosol number concentrations nudged to the Goddard Chemistry Aerosol Radiation and Transport (GOCART) model (Ginoux et al., 2001) based climatological data set described in Thompson and Eidhammer (2014). Additional physics parameterizations used include the Mellor-Yamada-Nakanishi-Niino (MYNN) level 2.5 eddy diffusivity mass flux scheme (Nakanishi & Niino, 2006, 2009), the Noah land surface scheme (Tewari et al., 2004), the Eta surface layer scheme (Janjić, 1994; Monin & Obukhov, 1954), and the Rapid Radiative Transfer Model for General Circulation Models (RRTMG; Iacono et al., 2008) with aerosol interactions included.

To match the observational temporal frequency, 15-min model output is used. Simulated radar reflectivity is computed from predicted hydrometeor size distributions assuming Rayleigh scattering, following Smith (1984). Top-of-atmosphere infrared brightness temperature (TOA IR T_b) is computed from outgoing broadband longwave radiation using the empirical relationship in Yang and Slingo (2001). Atmospheric sounding parameters are computed at both the observing site and at the cell initiation (CI) locations of individual tracked convective cells using methods consistent with the calculated parameters from observed soundings.

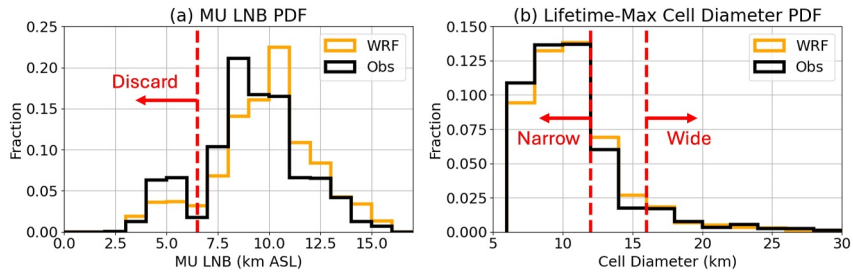

Figure 2. (a) Observed and simulated probability distributions of MU LNB at each cell's initiation time prior to filtering of samples for full life cycles and MU LNB > 6.5 km. (b) Observed and simulated probability distributions of cell lifetime-maximum diameter following filtering of samples with narrow and wide cell definitions shown based on the area-equivalent circle diameter.

3. Methodology

Observed and simulated convective cells are defined and tracked using PyFLEXTRKR (Feng et al., 2023) applied to composite (i.e., column-maximum) radar reflectivity in a consistent manner following Feng et al. (2022) with parameters tuned to work with 3-km horizontal grid spacing. Methodological details of how cells are identified and tracked are provided in Text S1 in Supporting Information S1. Many cell track statistics are saved for each time in a cell's life cycle including location, area, depth, and a range of radar-derived variables. Cell width is defined as the diameter of a circle with area equivalent to that of the cell mask. Cell depth is defined using two proxies: (a) 10-dBZ echo top height (ETH) and (b) minimum TOA IR T_b. The atmospheric parameters in Table 1 computed from observed soundings and simulated vertical profiles at both the observing site and CI locations are tagged to each cell track at the CI time and for the 60 min prior to it. Although it would be ideal to track atmospheric conditions surrounding each cell as it evolves in time, the limited temporal resolution of observations fixed at a single site does not allow this. Tracking of conditions along tracks in simulations is left for future work to determine how spatiotemporal sampling of atmospheric conditions relative to evolving cells affects the maximum depth that they reach.

Some cells are removed from analyses for various reasons. Cells to the west of 64.9°W are excluded due to low-level radar blockage by the mountains (Figure 1); 38.9% of observed cells and 41.6% of simulated cells are removed. In addition, cells with MUCAPE = 0 or MU LNB < 6.5 km ASL at the observing location are excluded, which removes another 7.2% of observed and 4.9% of simulated cells. MU LNB = 6.5 km is chosen as a lower threshold because it is a relative minimum in the MU LNB probability distributions, where values greater than it allow for the potential of deep convection (Figure 2a). To ensure complete cell life cycles, cells that begin as splits from a preexisting cell or end by merging with another cell are also excluded. This removes an additional 22.8% of observed and 28.2% of simulated cells, such that ~31% of the initial observed and ~25% of the initial simulated cell populations are retained. Retained cells are partitioned into narrow (<12 km) and wide (>16 km) diameter groups (Figure 2b). These thresholds are determined based on approximate diameters at which the relative importance of atmospheric predictors shifts in multiple linear regressions used later, which varies from 12 to 16 km depending on the data set (Figure S1 in Supporting Information S1). How this importance is computed is discussed further in Section 4.3. This partitioning corresponds to cell areas with 12 or fewer grid points for narrow cells and 23 or more grid points for wide cells. This results in 1,164 narrow and 125 wide observed cells, and 2,415 narrow and 268 wide simulated cells. Thus, there is a factor of ~2 overprediction of the total number of cells by WRF. The reasons for this overprediction are beyond the scope of this study but are shown by Zhang et al. (2024) not to be a result of insufficient model resolution. Rather, they hypothesize it to be related to biases endemic to physics parameterizations that require further investigation. Regardless, the observations and simulation both yield a similar factor of ~9 more narrow cells than wide cells. Because realistic cell areas can substantially deviate from circular shapes (Figure S2a in Supporting Information S1), analyses were also performed where the cell area-equivalent circle diameter is replaced by minor axis length of an ellipse fitted to each cell mask with the same area as the mask, where narrow and wide are defined as lifetime-maximum minor axis length <10 km and >13 km, respectively (Figure S3 in Supporting Information S1). Results using minor axis length to separate narrow and wide cells are very similar to those using diameters (Text S2 in Supporting Information S1).

4. Results

4.1. Comparison of Observed and Simulated Convective Cell Properties

The WRF simulation reasonably reproduces the MU LNB and cell diameter probability distributions (Figure 2). Cell lifetimes are also well simulated including the difference between narrow and wide diameter cells (Figures 3a and 3b). Narrow cell median lifetime is 30–45 min with very few samples reaching 2 hr, whereas wide cell median lifetime is 90 min with many cells exceeding 2 hr. Narrow cell lifetime-maximum radar reflectivity is also well simulated with only two dBZ separating observed and simulated median values (30 vs. 32 dBZ; Figure 3c). Wide cells have much greater lifetime-maximum radar reflectivity values with median observed and simulated values around 55 dBZ (Figure 3d). However, there are some differences in the wide cell reflectivity distributions. WRF has many cells with maximum reflectivity >60 dBZ, which is rare in observations. This difference may be reconciled by WRF reflectivity assuming Rayleigh scattering whereas observed C-band reflectivity may be affected by non-Rayleigh scattering by hail in intense storms that would lower reflectivity.

Median lifetime-maximum 10-dBZ ETHs for narrow cells are about 2.5 km higher in observations than WRF, while wide cell median ETHs are almost 5 km higher (Figures 3e and 3f). Despite this, median lifetime-maximum 10-dBZ ETH is 5 km higher for wide than narrow cells in both observations and WRF. Lifetime-minimum TOA IR T_b also exhibits a sizeable shift in values between narrow and wide diameter cells, with wide ones having 35–40°C colder median cloud tops (Figures 3g and 3h). Observed and simulated IR T_b distributions are closer to one another than ETH distributions if assuming reasonable moist adiabatic lapse rates for cell top temperatures and pressures. Observed narrow cell median values are about 8°C colder than simulated (Figure 3g; ∼1.3 km assuming a middle tropospheric lapse rate of ∼6°C km^{-1}), and wide cell median values are 4°C colder than simulated (Figure 3h; ∼0.4 km assuming an upper tropospheric lapse rate of ∼9°C km^{-1}). The weakness of IR T_b as a measure of cell top height is that anvils from deep cells can obscure shallower cells. However, a weakness of 10-dBZ ETH is that 10 dBZ can be well below cloud top. In addition, nonuniform radar beam filling and the radius of influence the Cartesian gridding algorithm used to fill in gaps between radar beams extrapolate echoes to higher altitudes than they realistically reach. Indeed, observed ETHs regularly exceed the sounding-estimated MU LNB and 0°C heights for a given minimum IR T_b by several kilometers (Figure S4 in Supporting Information S1). This phenomenon is not reproduced in the simulation; thus, observed ETHs are biased high. It is also possible that the simulation has a slight low bias in cloud top heights consistent with slightly warmer IR T_b values, which could also contribute to model-observation ETH differences. Despite such issues, the magnitude of the ETH distribution shift between narrow- and wide-diameter-observed cells is similar to that in the model. Because ETH biases likely cannot be fully removed with common Cartesian gridding techniques used here and due to the presence of nonuniform beam filling, we choose to move forward with the current ETH data set, using IR T_b analyses as context.

4.2. Convective Cell Correlations With Atmospheric Conditions

Correlations between atmospheric parameters and cell properties are examined for wide cells (Figure 4) and narrow cells (Figure 5) to assess which variables strongly covary and which parameters have the most significant relationships with cell depth. To provide less skewed distributions, MUCAPE and MUCIN variables are transformed from units of J kg^{-1} to m s^{-1} by assuming all potential energy is converted into kinetic energy. Because radar volumes were only available every 15 min, most narrow cells were only observed for a few time steps (30–45 min lifetimes), which introduces substantial uncertainty into the estimates of their lifetime-maximum depths reached. This likely limits correlation coefficient magnitudes and the accuracy of regressions in Section 4.3, but significant statistical relationships with atmospheric variables are still obtained due to sufficient sample sizes. Sensitivity to data set resolution is beyond the scope of this study but should be explored in the future.

Focusing first on correlations between cell properties, lifetime-maximum 10-dBZ ETH is highly correlated with lifetime-minimum TOA IR T_b, both being metrics for the cell depth reached, though correlations are notably higher for wide cells ($r = 0.76$–0.83) than narrow cells ($r = 0.56$–0.65) and a bit lower in observations ($r = 0.56$–0.76) than WRF ($r = 0.65$–0.83). That these correlations are not greater for two variables quantifying the cloud top demonstrates the uncertainty present in such metrics. Such uncertainty lowers correlations with other variables and supports the usage of multiple cloud top metrics to increase confidence in results. Cell lifetime-maximum radar reflectivity also positively correlates with cell depth metrics ($r = 0.36$–0.77) and cell lifetime, though cell lifetime is only weakly positively correlated with cell depth. Cell lifetime-maximum diameter

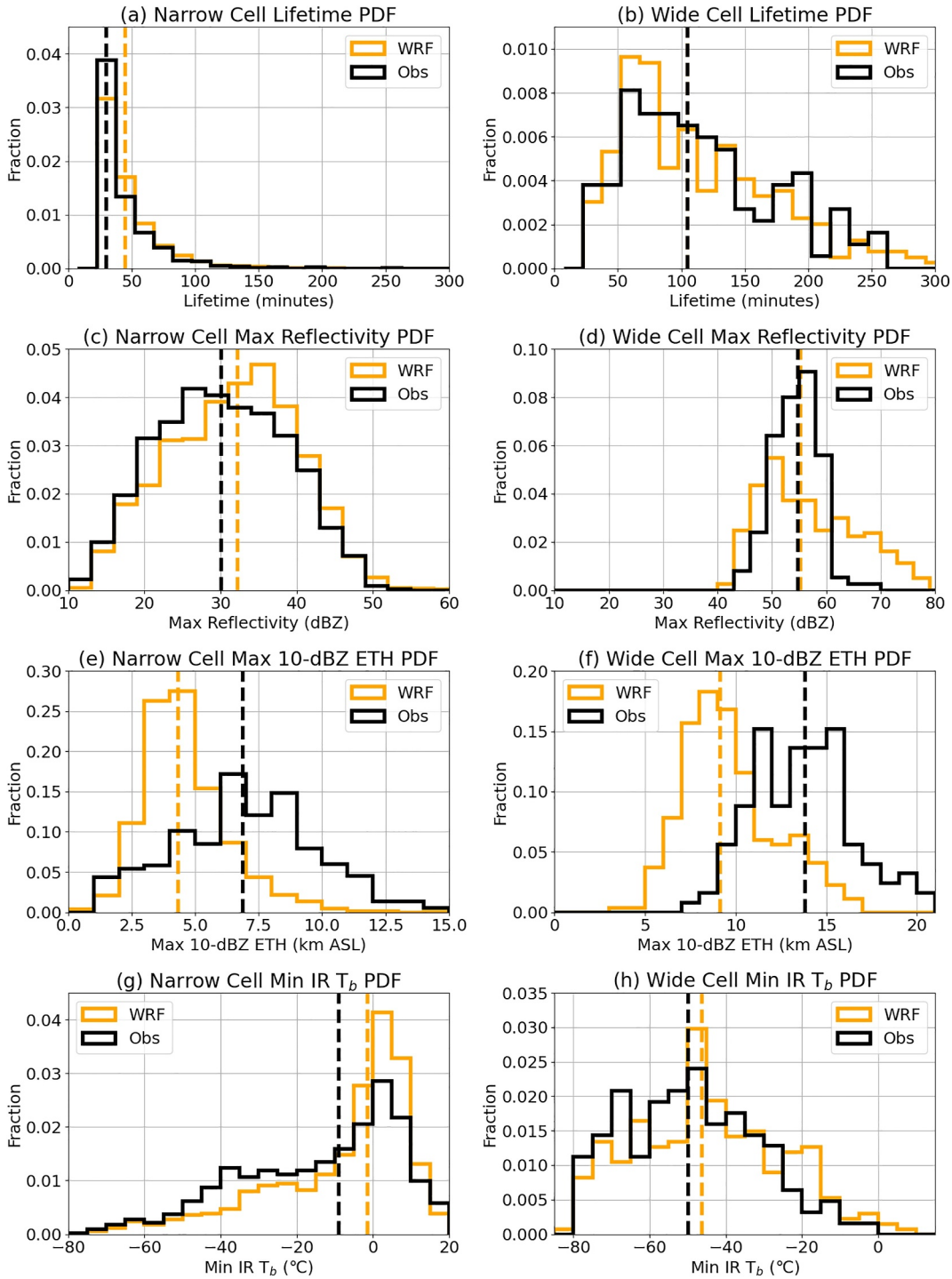

Figure 3. Observed and simulated probability distributions of cell (a–b) lifetime, (c–d) lifetime-maximum radar reflectivity, (e–f) lifetime-maximum 10-dBZ ETH, and (g–h) lifetime-minimum TOA IR T_b for (a, c, e, and g) narrow and (b, d, f, and h) wide cells. Dashed lines represent median values.

positively correlates with cell depth, maximum reflectivity, and lifetime for both narrow and wide categories ($r = 0.16$–0.55). Thus, grouping cells into narrow and wide diameter categories does not completely control for cell diameter effects on cell depth, which is expected but unavoidable given the need for sufficient sample sizes within width categories.

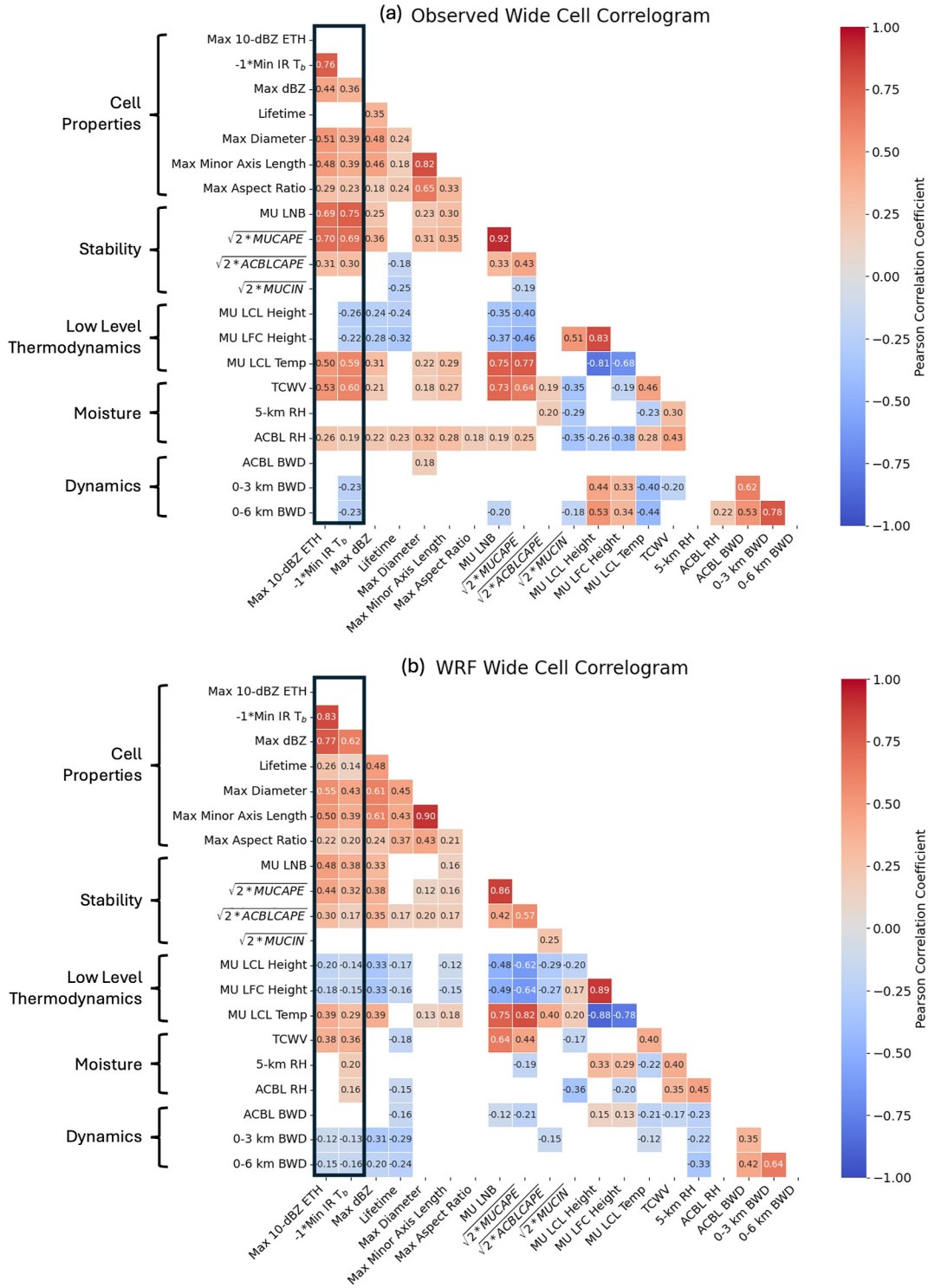

Figure 4. Pearson correlation coefficients of wide cell properties with one another and atmospheric parameters at cell initiation and the observing site for (a) observations and (b) WRF. Color filled boxes are statistically significant at a 5% level. The first two columns show correlations with cell depth variables with minimum TOA IR T_b reversed in sign to match maximum 10-dBZ ETH.

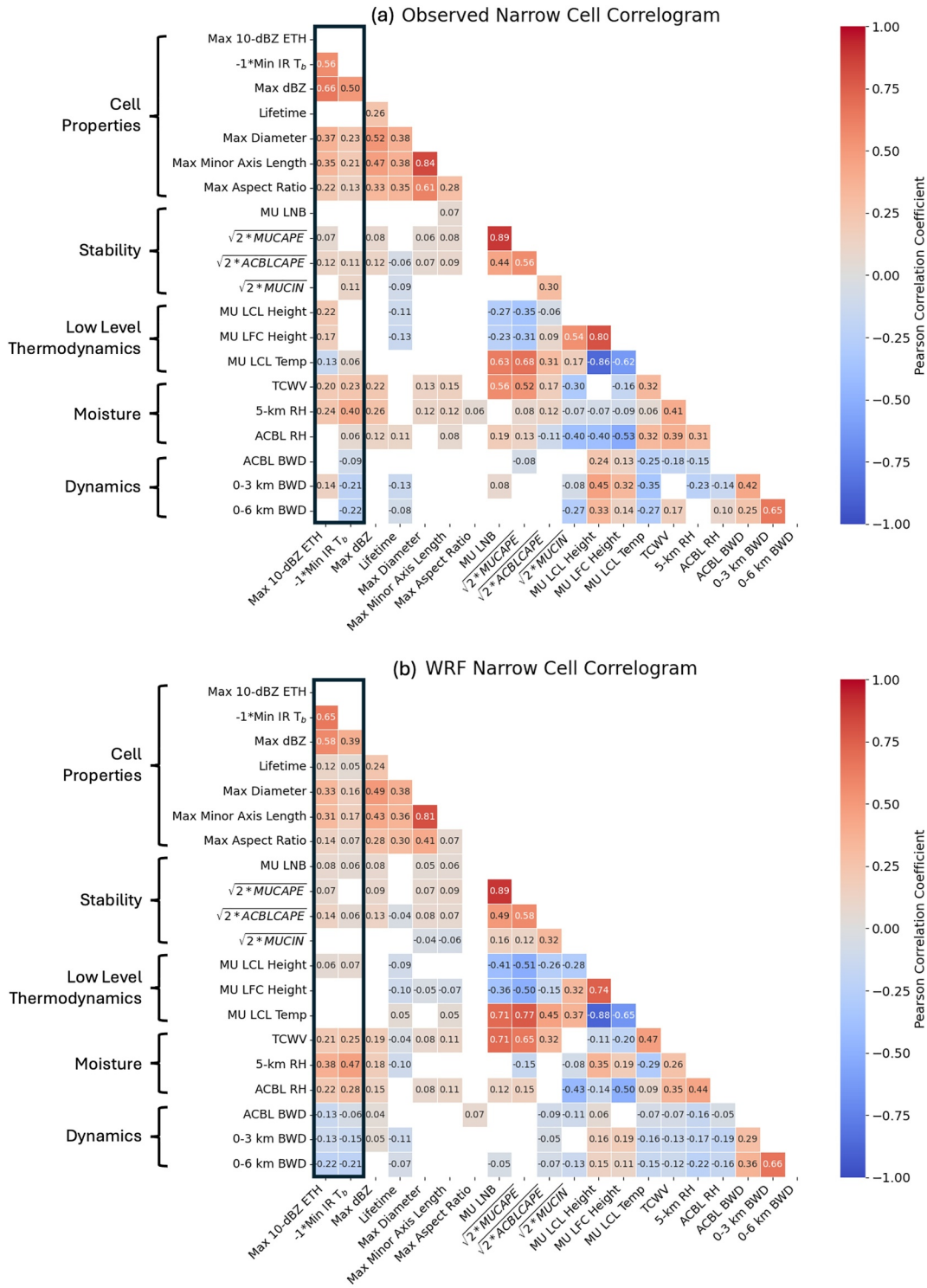

Figure 5. Following Figure 4 but for narrow cell properties for (a) observations and (b) WRF.

Correlations between sounding-derived parameters and the two cell depth metrics (first two columns of Figures 4 and 5) are clearly different between narrow and wide diameter cell groups with correlations generally consistent between observations and WRF. Wide cell maximum depth (ETH and IR T_b) best correlates with instability parameters (MU LNB, r = 0.38–0.75; MUCAPE, r = 0.32–0.70) and secondarily correlates with TCWV (r = 0.36–0.60) and MU LCL temperature (r = 0.29–0.59), with greater correlations for observations than WRF.

These variables also strongly correlate with one another, indicating redundant information between them. Narrow cell maximum depth also positively correlates with TCWV (r = 0.20–0.25). However, in contrast to wide cells, narrow cell depth has very weak or insignificant correlations with MU LNB, MUCAPE, and MU LCL temperature. Instead, 5-km RH correlates most strongly with narrow cell depth (r = 0.24–0.47) with greater correlations in the model than observations. Other parameters have inconsistent correlations with narrow cell depth apart from a negative correlation with 0–6 km bulk wind difference in the simulation (r = −0.21, −0.22) and in observations for minimum TOA IR T_b (r = −0.22). 5-km RH and TCWV also positively correlate with one another, indicating some redundancy in their information, though their correlation is weaker than those between the top wide cell depth predictors (TCWV, MU LNB, MUCAPE, and MU LCL temperature). These correlations only slightly change for the simulation when using sounding-derived parameters from CI locations 15 min prior to CI rather than parameters at the fixed observing site at CI time (Figure S2 in Supporting Information S1). Maximum cell depth metrics also positively correlate with the maximum cell aspect ratio (r = 0.07–0.29) and minor axis length (r = 0.17–0.50), more for wide than narrow cells. However, the correlations with minor axis length are very similar to those with diameters because of their high correlation. Indeed, correlograms using minor axis length to define narrow and wide groups are very similar to those using diameter (Figures S6 and S7 in Supporting Information S1).

4.3. Atmospheric Predictors of Cell Lifetime-Maximum Depth

Because of covariabilities between atmospheric predictors of lifetime-maximum cell depth, multivariate linear regressions (MLRs) of maximum 10-dBZ ETH and minimum TOA IR T_b against sounding-derived parameters are performed to better isolate individual relationships. To limit predictor covariability, some predictors shown in Table 1 and Section 4.2 are removed from the MLR. We first remove the ACBL variables (CAPE, RH, and BWD) because they do not contribute to predicting depth in an MLR including all predictor variables as much as their counterparts not limited to the ACBL (MUCAPE, 5-km RH, 0–6 km BWD). TCWV is also removed because it correlates with other more dominant moisture and instability variables and can also affect cell depth through multiple pathways, which makes interpretations ambiguous. MU LNB, MUCAPE, and MU LCL temperature also highly correlate with one another; thus, LCL temperature is removed because its effect on depth is more ambiguous than MU LNB and MUCAPE. Both MUCAPE and MU LNB are retained despite being strongly correlated because either can be a better predictor of the two depending on the depth proxy used. Finally, the number of predictors is then further reduced by removing any that do not contribute significantly to both narrow and wide diameter cell depth prediction for both observations and WRF. This criterion removes MUCIN and MU LFC height. MU LCL height is retained despite statistically significant negative correlations with MU LNB and MUCAPE because of its importance in predicting observed depths discussed below. Reasons for this negative correlation are unclear but could be related to (a) deeper boundary layer mixing lowering LNB and CAPE values while increasing LCL heights, and/or (b) inclusion of elevated convection environments that have relatively high LCL heights with lesser CAPE over shallower layers than moist convection rooted in the boundary layer. The reduction in the number of predictors slightly lowers the MLR r^2 values but improves interpretation with limited predictor covariability (apart from LNB and CAPE) and physically justifiable coefficient signs except for the balance between highly correlated MU LNB and MUCAPE variables.

Figure 6 shows the percentage that each retained sounding-derived parameter contributes to the MLR r^2 values for predictions of cell lifetime-maximum depths. These are computed via Shapley regression, which computes r^2 contributions of each regression predictor by computing an MLR r^2 value for every possible combination and ordering of 1 to all (5 in this case) predictors, assessing how MLR r^2 values change based on inclusion or exclusion, and ordering, of each predictor. These changes are then averaged for each predictor to come up with the predictor contribution to the overall MLR r^2 value using all five predictors, following Lindeman et al. (1980). The r^2 contributions here are converted to percentages of the total r^2 for easier interpretation. These values are often referred to as the "importance" of each predictor. Predictor r^2 contributions generally follow the ordering of individual parameter correlations in Figures 4 and 5 because of the limited covariability between predictors (Figures 4 and 5). Because of this, the dominant MLR predictors of lifetime-maximum 10-dBZ ETH and lifetime-minimum TOA IR T_b are the variables that correlate the most with ETH and IR T_b. For both observed and simulated wide cells, this is MU LNB and MUCAPE, with MU LNB having more contribution to IR T_b and each contributing similarly to ETH. Depending on the data set, MUCAPE and MU LNB combine to contribute 66%–94% of the total r^2 for wide cells. Other variables with statistically significant coefficients provide lesser

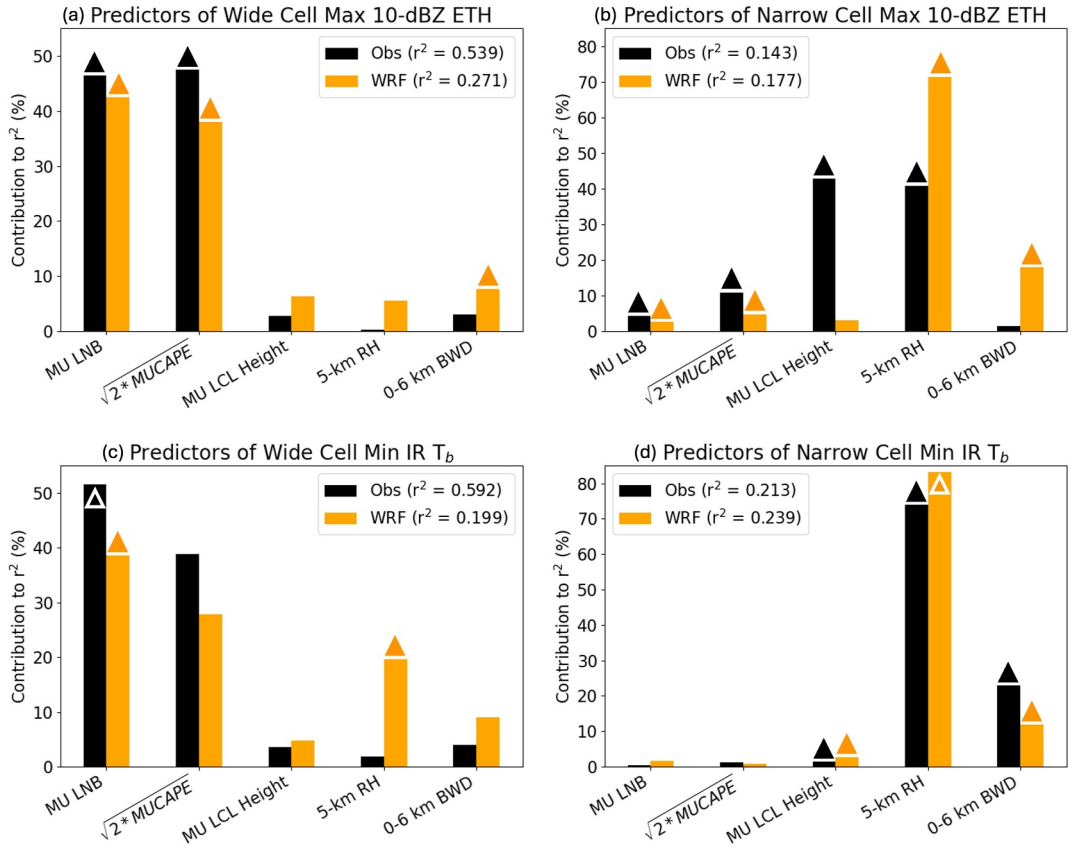

Figure 6. Observed and WRF predictor contributions to the coefficient of determination (r^2) for lifetime-maximum 10-dBZ ETH for (a) wide and (b) narrow cells, and lifetime-minimum TOA IR T_b for (c) wide and (d) narrow cells. Triangles indicate statistically significant predictors at a 95% level. r^2 value in the legends correspond to each MLR using all predictors shown together.

contributions, particularly MU LCL height for observations (3%–6%) and both 0–6 km BWD (3%–9%) and 5-km RH (0%–20%) for WRF. Because MU LNB and MUCAPE are highly correlated, additional regressions were also performed with one or the other removed. Doing so substantially increases the importance of the variable retained, ensuring statistical significance for the retained variable while only minorly lowering the overall r^2 values (Figures S8 and S9 in Supporting Information S1). For both observed and simulated narrow cells, 5-km RH is the dominant predictor with 41%–83% contribution to r^2. For lifetime-minimum TOA IR T_b, observed and simulated contributions are very similar, with a secondary contribution from 0 to 6 km BWD (12% for WRF, 23% for observations). For lifetime-maximum 10-dBZ ETH, the 5-km RH contribution is much lower for observations (41%) than WRF (72%) due to a 43% contribution from MU LCL height. It is unclear why MU LCL height is more important in observations than WRF, but some speculation is provided later. 0–6 km BWD is the second most important WRF predictor (18%), while MU LNB and MUCAPE also provide minor (<11%) contributions to both observed and simulated narrow cell ETHs.

Except for observed wide cells, MLR r^2 values are rather limited (Figure 6). This is somewhat expected due to several factors. First, the MLR model is valuable because it can identify statistically significant relationships that are physically interpretable in support of our primary objectives using observable metrics. However, because it is based on linear combinations of predictors, it may not fully capture more complex nonlinear relationships. Second, observational sampling limits accuracy. For example, the depth reached by cells is crudely approximated using 15-min temporal resolution and imperfect proxies (ETH and IR T_b). Further, atmospheric conditions tagged to each cell at CI time may not adequately represent those experienced by each cell's updrafts. Observed conditions are limited by interpolating between 3-hourly radiosonde measurements from a single location. Furthermore, assumptions are required to obtain lifted parcel metrics (here, the most unstable parcel without consideration of mixing, condensate loading, or freezing) that are likely variably relevant for any given updraft.

Third, there are nonsounding-based factors unaccounted for in the MLR, including cloud microphysical effects and interactions among neighboring cells. Adding cell lifetime-maximum diameter (shown later to be proportional to updraft area-equivalent circle diameter) as a predictor in each cell width group substantially increases r^2 values for maximum 10-dBZ ETH and wide cell predictions, with lesser increases for narrow cell minimum TOA IR T_b (Figure S10 in Supporting Information S1). Despite the importance of cell diameter to predicting cell depth, the relative contributions of sounding-derived atmospheric parameters at the time of CI at the observing site location remain mostly unchanged from the MLR that excludes it in Figure 6. The lifetime-maximum cell diameter is also undermined as a predictor because it can also respond to cell depth, an issue that is discussed further in the conclusions. The impact of fixed site conditions for variable cell locations is tested by performing regressions on simulated cells using conditions at the CI locations 15 min prior to CI to avoid contamination by the growing cell prior to detection of its reflectivity signature used to define a cell. Changing sounding sampling locations minorly increases r^2 values, and the relative importance of predictors remains mostly unchanged with only slight increases in the importance of MUCAPE and 5-km RH (Figure S11 in Supporting Information S1). Using cell lifetime-maximum minor axis length rather than lifetime-maximum diameter to characterize cell width also results in little change to the relative importances of predictors and no improvement in overall r^2 values (Figure S12 in Supporting Information S1). Further discussion of the relative accuracies of the various MLR predictions is provided with Text S3 in Supporting Information S1.

MLR coefficients provide the sensitivity of maximum cell depth to each predictor (Figure 7). Standardized coefficients are shown such that the magnitudes can be compared across predictors. These can be interpreted as the number of standard deviations that the depth proxy (ETH or IR T_b) will change given a standard deviation change in the predictor variable where the standard deviations are dictated by the distributions of variable values in each data set.

The greater importance of instability metrics (MU LNB and MUCAPE) for wide cells than narrow cells is apparent with greater coefficient values that are positive, indicating more instability over a greater depth leads to greater cell depths. Because MU LNB and MUCAPE contain redundant information, their coefficient magnitudes are more uncertain than other variables and either can have statistically insignificant signs (Figure 7). Similar to r^2 contributions (Figure 6), it is apparent that MUCAPE and MU LNB are similarly important predictors for wide cell lifetime-maximum ETH, whereas MU LNB matters more for simulated wide cell IR T_b. Interestingly, MU LNB and MUCAPE have significant coefficient values for narrow cell ETH, but the MUCAPE coefficient is positive, and the MU LNB coefficient is negative. This suggests that focusing CAPE into a thinner layer is beneficial to narrow cell deepening, which is physically plausible in that this increases undiluted buoyancy over the CAPE containing layer such that the updraft is better protected from depletion of buoyancy to entrainment-driven dilution (e.g., Houston & Niyogi, 2007). Consistent with this idea, ACBL CAPE, which is computed over a fixed 1.5-km depth directly above the LFC, is a better predictor for narrow cell depth than MUCAPE and MU LNB (Figure 5). In addition, removing either MUCAPE or MU LNB as a predictor results in small and certain (small confidence interval) positive coefficients for narrow cells for the retained predictor (Figures S13 and S14 in Supporting Information S1), indicating the large narrow cell coefficients for maximum ETH in Figure 7a result because of counteracting MUCAPE and MU LNB effects. Removing either MU LNB or MUCAPE also increases the retained predictor coefficient magnitudes for wide cells with all becoming statistically significant and similar in value for a given data set, though cell depth sensitivities to these instability metrics are greater in observations (>0.7) than WRF (<0.6). Also consistent with the r^2 contributions, 5-km RH coefficients are positive and greater for narrow cells than wide cells, indicating greater midlevel RH supports narrow cell deepening with slightly greater sensitivity in WRF than observations.

Of the remaining predictors, MU LCL height has significant, positive coefficient values for observed narrow cells such that higher LCLs are associated with deeper cells, potentially via increases in cloud base updraft width (e.g., Mulholland et al., 2021; Takahashi et al., 2023). However, MU LCL height is not important in the simulation. This may be due to 3-km grid spacing's inability to fully resolve updraft width in narrow cells, making many updrafts wider than they would be in the real world (see references in Section 1). The 0–6 km BWD coefficients are negative for narrow cells, meaning increases in deep vertical wind shear are associated with decreases in cell depth. For narrow cells, this is physically reasonable as vertical wind shear can enhance entrainment (see references cited in Section 1). Wide cells should be more resistant to this effect, perhaps contributing to three of four coefficients being statistically insignificant. Sampling of wide cells being much more restricted than narrow cells also renders wide cell predictors more uncertain as evidenced by much larger confidence intervals for wide as

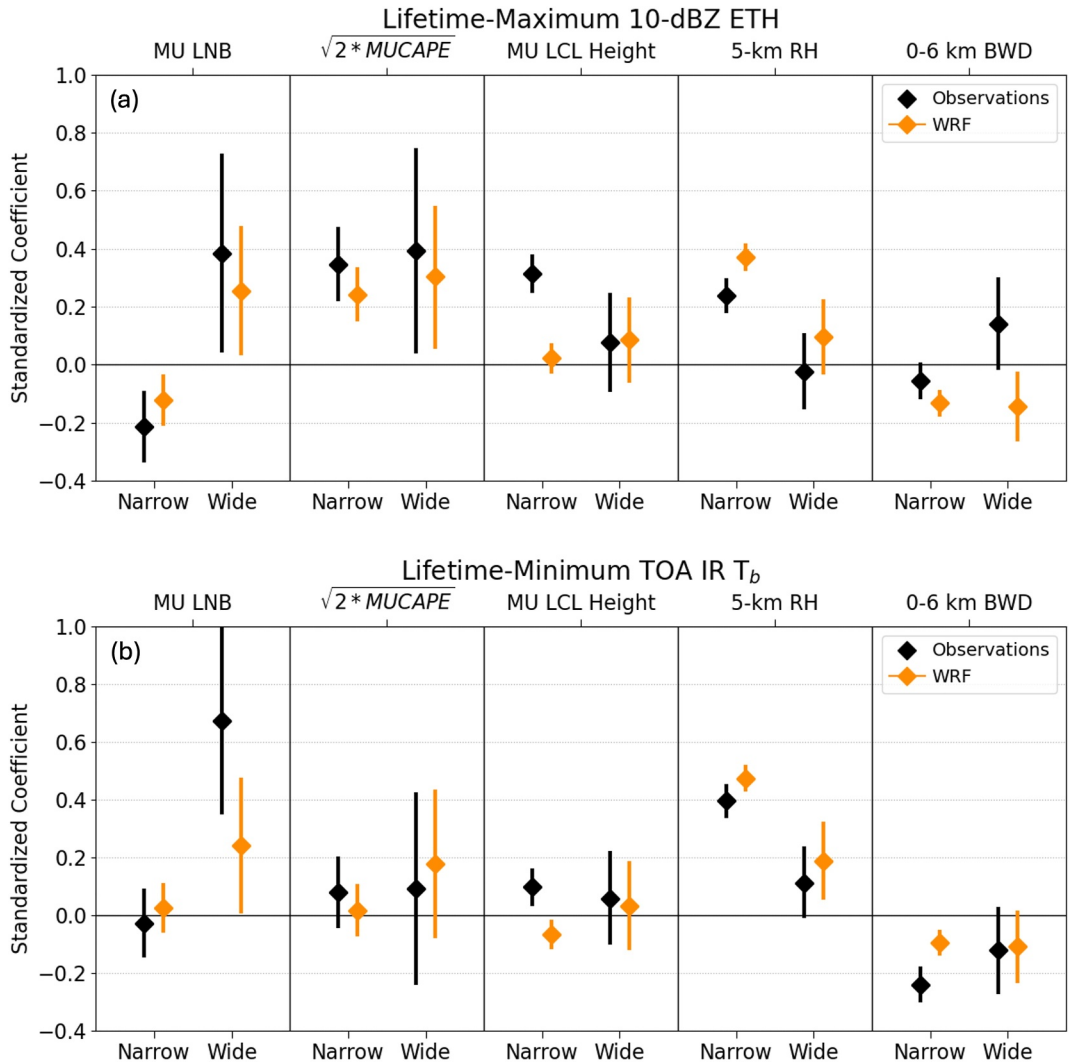

Figure 7. Observed and simulated multivariate linear regression predictor standardized coefficients with 95% confidence intervals for narrow- and wide-diameter cells (a) lifetime-maximum 10-dBZ ETH and (b) minimum TOA IR T_b. Confidence intervals are computed from the MLR standard error.

compared to narrow cells in Figure 7. Larger sample sizes in future studies would lessen uncertainty and potentially allow for the determination of the signs of secondary predictors and more robust quantification of sensitivities.

Including cell lifetime-maximum diameter as an additional predictor shows that increases in the cell diameter are unsurprisingly associated with increases in cell depth, with similar coefficient magnitudes in WRF and observations (Figure S15 in Supporting Information S1). Despite the addition of the cell diameter and increase in predictive skill, coefficient magnitudes for the other predictors do not significantly change. This is again consistent with the r^2 contribution analyses and suggests that controlling for the diameter within narrow and wide diameter cell groups does not affect assessment impacts of ambient meteorological conditions on cell deepening. Using predictor values from CI locations 15 min prior to CI in the simulation also does not significantly change coefficients, with the exception that MUCAPE becomes more important and MU LNB less important (Figure S16 in Supporting Information S1). This is consistent with the decrease in correlation of MU LNB and increase in correlation of MUCAPE with depth proxies for wide cells (Figure S5 in Supporting Information S1 vs. Figure 4). Lastly, using minor axis length instead of the diameter to define narrow and wide cell groups results in very little changes to predictor coefficients (Figure S17 in Supporting Information S1).

4.4. Cause of Differing Narrow and Wide Cell Sensitivities to Atmospheric Conditions

Given the overall success of the WRF simulation in reproducing observed relationships, we further interrogate the apparent cell diameter modulation of thermodynamic controls on cell depth in the simulation. The time evolution of the atmospheric thermodynamic vertical structure leading up to CI showcases the vast differences between narrow and wide diameter cell depth sensitivities (Figures 8 and 9).

Wide cells that become deep are associated with environments containing higher θ_e throughout the atmosphere than for wide cells that remain shallow. This is especially true in the lower troposphere, where deep θ_e is more than 5 K greater both at CI locations (Figure 8a) and the fixed observing site (Figure 8b) because the atmosphere is warmer by up to 4 K (Figures 8c and 8d) and moister by up to 2 g kg^{-1} (Figures 8e and 8f). These differences are present 1 hr before CI with little change leading up to it. While conditions at the fixed observing site appear sufficient to statistically separate shallow and deep atmospheric conditions, water vapor mixing ratio differences between shallow and deep conditions are even greater at CI locations. Figure S18 in Supporting Information S1 shows the same time-heights as Figure 8 but using lifetime-minimum TOA IR T_b rather than lifetime-maximum 10-dBZ ETH as the maximum depth proxy to separate shallow and deep wide cells. It generally shows the same difference in thermodynamic structure between shallow and deep cell median conditions.

Contrary to the wide cell population, narrow cells that become deep are associated with lower θ_e in the lower troposphere than those that remain shallow. Instead, deep narrow cells have greater θ_e values in the mid-troposphere between 4 and 6 km ASL (Figures 9a and 9b). This structure is dominated by water vapor differences (Figures 9e and 9f) with up to a 1.5 g kg^{-1} greater mixing ratio between 4 and 5 km ASL at CI locations for narrow cells that become deep relative to those that remain shallow (Figure 9e). This same 4–5 km layer is also cooler by about 1 K at CI locations for cells that become deep (Figure 9c). The same thermodynamic vertical structure difference between shallow and deep narrow cells is apparent at the fixed observing site but with lesser magnitudes (Figures 9b, 9d, and 9f). Using lifetime-minimum TOA IR T_b as the cell depth proxy presents a similar picture with deeper narrow cells experiencing moister and cooler midlevels but cooler and drier low levels (Figure S19 in Supporting Information S1). Similar to wide cell conditions, thermodynamic differences are clearly present at least 1 hr before CI and change very little leading up to it.

Combined with the representativeness of the fixed observing site for CI locations that vary out to 100 km away from the observing site, the presence of differences 1 hr ahead of CI suggests that mesoscale and synoptic-scale conditions rather than near-cloud conditions are a primary regulator of the probability for both narrow and wide diameter cells to deepen. Indeed, free tropospheric subsidence above 3 km ASL is greater at the observing site for shallow than deep narrow cells (Figure S20 in Supporting Information S1). This difference disappears at CI locations where the primary difference is deeper low-mid level ascent prior to CI extending to 5-km ASL for deep narrow cells as compared to only 3-km ASL for shallow narrow cells. This suggests that cloud-scale to mesoscale ascent processes at the CI location also potentially influence narrow cell depth. Wide cells, on the other hand, exhibit little discernable vertical motion differences for shallow and deep outcomes (Figure S21 in Supporting Information S1), suggesting horizontal advection and/or surface fluxes regulate the large-scale thermodynamic stability that exerts the most dominant control on the cell depth reached.

The strong relationship between midlevel RH and the depth reached by narrow cells (but not wide cells) is consistent with the idea that updrafts become less sensitive to entrainment-driven dilution as they widen. For this to be true, cell updraft width would need to strongly correlate with cell width. This cannot be examined in observations, but it can be examined using model output. Indeed, cell lifetime and the column-maximum updraft diameter used to represent width is highly correlated with the lifetime-maximum cell diameter ($r^2 = 0.59$; Figure 10), and the correlation is even greater for column-maximum cell area versus updraft area ($r^2 = 0.71$; not shown). Furthermore, if entrainment-driven dilution is a primary control on narrow cell depth, the vertical profile of updraft pseudoadiabatic θ_e should decrease more rapidly with height for shallow cells than deep cells. Figures 11a and 11c show that this is indeed the case in the WRF simulation. Narrow cell maximum θ_e decreases with height at a rate that is consistent with the decrease in minimum θ_e with height in the local vicinity of the cell updraft at CI. This suggests that the more rapid θ_e decrease in shallow, narrow cell updrafts is a result of the more rapid θ_e decrease outside the updraft (Figure 11a). This effect dominates over the apparent greater undiluted parcel instability for shallow, narrow cells associated with ~3 K greater starting θ_e values. For wide cells, the rate that ambient θ_e decreases with height is not greater in relatively shallow cells as compared to deep cells, indicating entrainment-driven dilution is a less significant determinant of wide cell depth. Instead, relatively wide

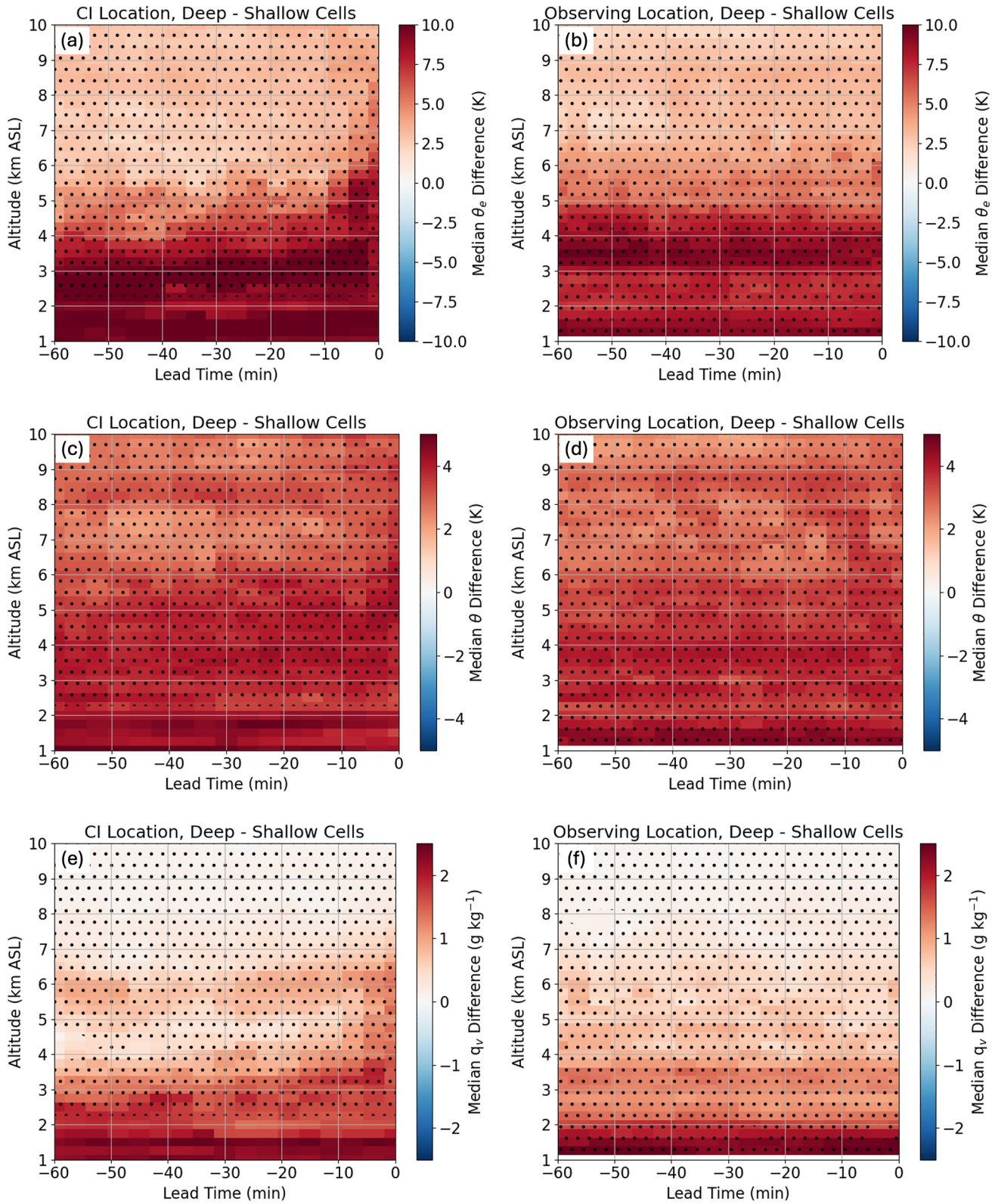

Figure 8. The difference in simulated median (a) pseudoadiabatic θ_e, (c) potential temperature (θ), and (e) the water vapor mixing ratio (q_v) at CI locations for deep and shallow (high minus low) maximum 10-dBZ ETH wide cells for the 1 hr leading up to CI. Deep and shallow are defined as greater and less than the wide cell median lifetime-maximum 10-dBZ ETH value, respectively. The dots indicate statistically significant differences at a 5% level using a Mann-Whitney U test. The same is shown in (b, d, and f) but for the fixed observing site rather than CI locations.

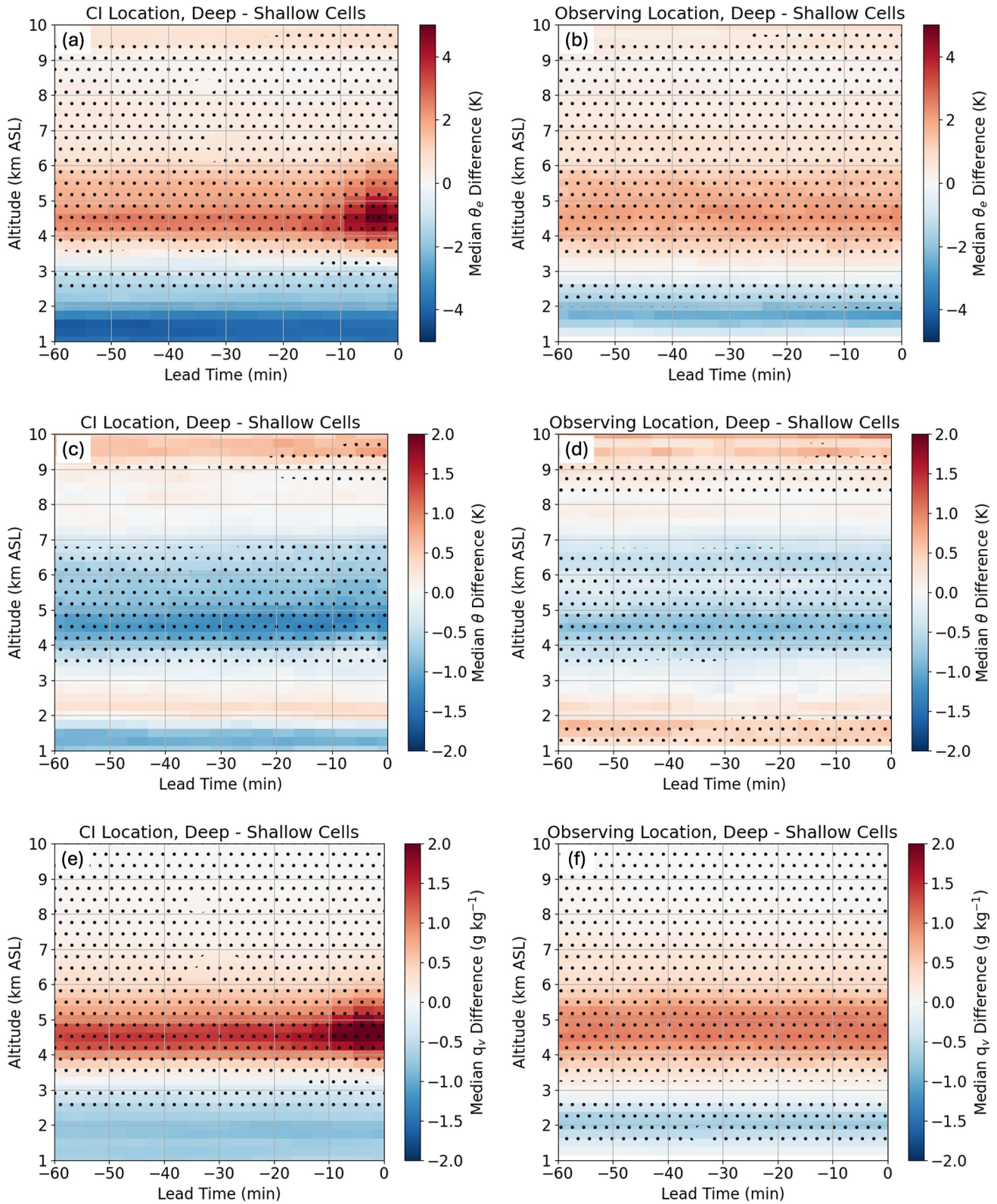

Figure 9. Following Figure 8 but for narrow cells.

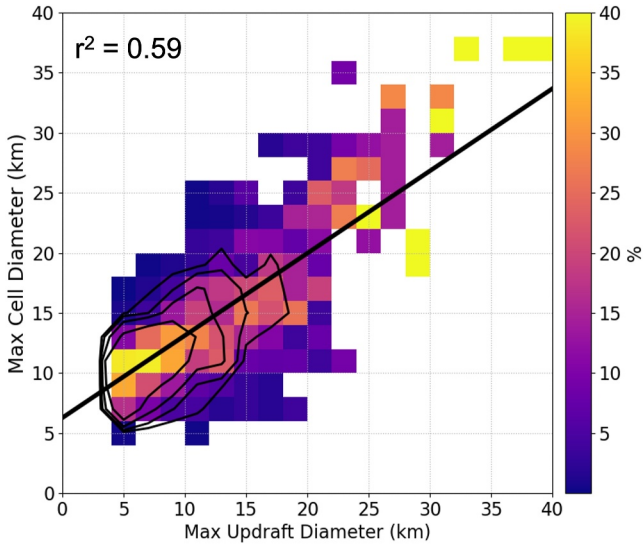

Figure 10. Frequency of WRF column- and lifetime-maximum cell diameters conditioned on column- and lifetime-maximum updraft diameters (color fill) with joint distribution frequency (black contours at 0.4%, 0.8%, 1.6%, and 3.2%) and a linear fit line (black). The updraft diameter at each height and time is defined as the diameter of a circle with area equal to the area of vertical motion >1 m s^{-1} within the cell mask.

cells become deeper in association with greater instability and higher undiluted parcel equilibrium levels, which are associated with 7 K greater starting θ_e values (Figure 11c). Similar results are found when using TOA IR T_b as the cell depth proxy (Figure S22 in Supporting Information S1).

5. Conclusions

This study quantified factors controlling the depths achieved by narrow and wide convective cells tracked at 15-min frequency between mid-October 2018 and early March 2019 in central Argentina using both CACTI observations and a WRF simulation with 3-km horizontal grid spacing. Cells were tracked using composite radar reflectivity, and a range of atmospheric parameters relevant to convective cloud growth were computed from observed and simulated soundings tagged to each cell at its initiation time. Each cell's lifetime-maximum depth was estimated by its lifetime-minimum TOA IR T_b as well as its lifetime-maximum 10-dBZ ETH. Cells were separated into narrow and wide groups based on their lifetime-maximum area-equivalent circle diameters, resulting in 1,164 narrow and 178 wide observed cells and 2,415 narrow and 447 wide simulated cells. The simulated cell number bias is explored further in Zhang et al. (2024). Multivariate linear regression was used to quantify atmospheric condition impacts on the observed and simulated maximum depths reached by cells conditioned upon the cells being narrow or wide. The predictor variables chosen were MU LNB, MUCAPE, 5-km RH, MU LCL height, and 0–6 km BWD. These variables consist of dominant individual predictors of maximum ETH or minimum IR T_b for either narrow or wide diameter cells plus select additional parameters that provided complementary predictive value across some or all the observed and simulated narrow and wide cell data sets.

Stark contrasts were found between the variables contributing most to predicted maximum depths for narrow versus wide cells. Wide cell maximum depth responded most to instability (MUCAPE and MU LNB) that is heavily modulated by low-level moisture variability. However, narrow cell maximum depth responded most to midlevel RH with mostly negligible contributions from MU LNB and MUCAPE apart from the requirement that they are sufficiently high to support the possibility of deep convection. These results were consistent for both metrics of cell depth (ETH and IR T_b). The simulation produced generally similar results to observations despite its relatively coarse 3-km horizontal grid spacing.

Examination of simulated cells confirms that the cell diameter strongly correlates with the updraft diameter, and narrow cell θ_e decreases with height at a rate similar to the minimum θ_e in the vicinity of the cell updraft. This indicates that *entrainment of ambient, drier air into updrafts primarily controls the depth reached by narrow cells with RH in the 4–6 km ASL layer mattering most*. Most of these cells fell substantially short of reaching the MU LNB, with sharp drops in the updraft maximum θ_e with height. Thus, *MU LNB and MUCAPE were not good predictors for narrow cell maximum depth*. However, *CAPE and LNB are very good predictors for wide cell maximum depth because updraft maximum θ_e decreases more slowly in their wide updrafts as compared to narrow cells with narrow updrafts such that wide cell depth is not very sensitive to midlevel RH and entrainment-driven dilution*. Wide cells that are shallower simply have less potential to become deep as quantified using undiluted lifted parcel metrics. There are many more relatively narrow cells than wide cells, which could explain why CAPE alone is often not a good predictor of a convective cell outcome (e.g., Igel & van den Heever, 2015; Louf et al., 2019; Mapes & Houze, 1992; Sherwood, 1999; Zipser, 2003).

These findings from observations and nonidealized simulations across many different cases and atmospheric conditions support previous idealized modeling and observational studies showing that convective cell depth is sensitive to free tropospheric RH and CAPE but with modulation by updraft width because of its regulation of entrainment-driven dilution of updraft buoyancy. However, this does not mean that the magnitudes of these sensitivities derived here are the same across studies, and further research is required to quantify convective cloud dependencies on atmospheric conditions. Indeed, some simulated and observed sensitivities in this study differ in magnitude despite the relative importance of predictors and the signs of sensitivities being generally similar.

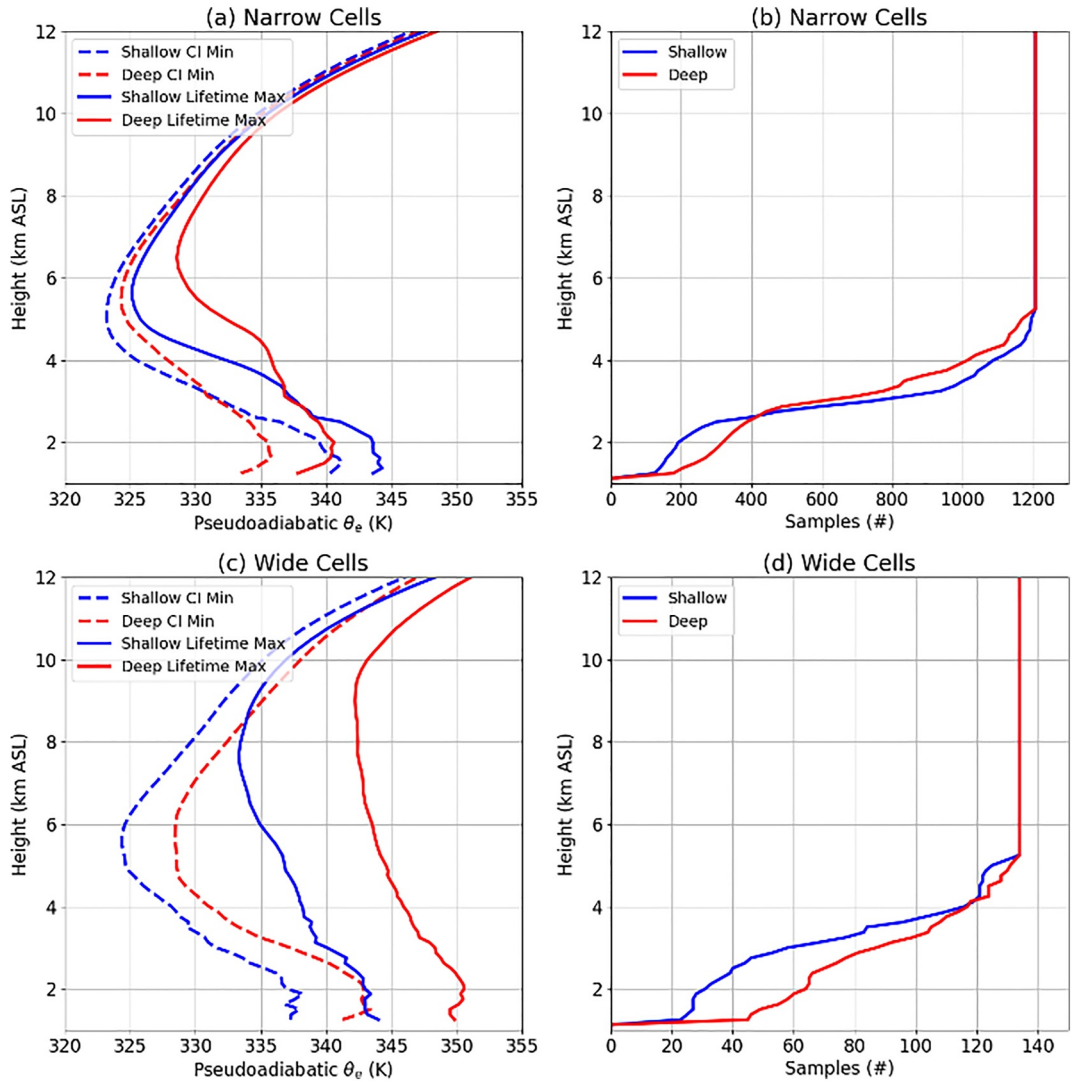

Figure 11. (a) Mean narrow cell lifetime-maximum pseudoadiabatic θ_e for shallow versus deep cells as determined from lifetime-maximum 10-dBZ ETH overlaid on the mean of minimum θ_e in the vicinity of cells at CI. Maximum θ_e is chosen to represent the most undiluted updraft air, and minimum θ_e at the CI time is chosen to represent the ambient conditions; the updraft is growing into with limited effects from the growing cell. Samples as a function of height are shown in (b). (c–d) Same variables as (a–b) but for wide cells. Deep and shallow for each of the narrow and wide diameter categories are defined as greater and less than the median lifetime-maximum 10-dBZ ETH value in each category, respectively. Values are only included at the most unstable height level and higher, resulting in the change in samples with height.

For secondary predictors, lesser 0–6 km BWD generally encourages deeper narrow cells, perhaps via detrimental entrainment and downward dynamic pressure gradient mechanisms (e.g., Nelson et al., 2022; Peters et al., 2019). The causes for a lack of a positive effect of 0–6 km BWD on wide cell depth following arguments of enhanced updraft inflow in Peters et al. (2022a, 2022b) are unclear but could be related to interactions between orographic forcing and BWD that affect local thermodynamic conditions at CI locations as well as cell motion and updraft inflow (e.g., Kirshbaum, 2011, 2013; Lareau et al., 2024; Nelson et al., 2022). Many cells were also fed by elevated instability with updrafts that would be more sensitive to elevated BWD layers rather than those starting at the surface that were assessed here. Although greater MU LCL height encourages deeper narrow cells in the observations, a similar signal is not found in the simulation. Greater MU LCL height may encourage wider updrafts via boundary layer thermal scaling arguments (e.g., Mulholland et al., 2021; Takahashi et al., 2023), but 3-km grid spacing likely cannot resolve such scaling. Additionally, when ETH is used as the depth proxy, narrow cells become deeper as MUCAPE increases and MU LNB decreases. Combined with a positive effect of ACBL

CAPE on narrow cell depth, this suggests that vertically concentrating instability into a thinner layer allows narrow updrafts to survive entrainment-driven dilution longer because they start with greater buoyancy. Further research is required to better isolate and quantify these secondary effects on convective cloud depth.

Using simulated atmospheric conditions from CI locations rather than the fixed observing site slightly improves regression accuracy, and further including lifetime-maximum diameter as a sixth predictor notably improves regressions. Separating cells into narrow and wide diameter bins does not control for cell and updraft width effects on deepening because of the strong sensitivity of depth to width. This is a weakness of using binning to control for a sensitive relationship (e.g., see Section 4 of Varble et al., 2023), but in this case, it does not meaningfully alter the relationships of maximum cell depth with the atmospheric predictors. Using the minor axis length of an ellipse fitted to cell masks as a measure of cell width produces very similar results to using a diameter of a circle with area equivalent to the cell area, indicating cells that deviate substantially from a circular footprint do not substantially affect our conclusions.

The simulation further shows that atmospheric state differences between shallow and deep cells exist 1 hr prior to cell initiation, change little leading up to initiation, and are generally represented at a fixed site within 100 km of CI locations. This suggests that mesoscale to synoptic scale circulations exert a substantial control on the local thermodynamic state affecting cell outcome probabilities. The strength of free tropospheric subsidence impacts narrow cell depth but not wide cell depth, which is instead regulated by lower tropospheric heat and moisture, presumably via horizontal advection and surface fluxes.

This study has several limitations and caveats that can potentially be addressed in future research. A foremost limitation is the assumption that lifetime-maximum cell depth responds to the lifetime-maximum updraft diameter and the atmospheric interactions that it modulates. However, deeper cells can be expected to produce larger reflectivity footprints as precipitation falls out over a broader area; thus, a diameter can also respond to depth. The 15-min output frequency is insufficient to examine such lead-lag relationships, which should be investigated with higher frequency model output and measurements in the future. 15-minute output also results in uncertain quantification of cell lifetime-maximum depths, uncertainty that could be explored with higher resolution data sets in the future. The need to use radar reflectivity to define and track cells in observations introduces further uncertainties. Reflectivity responds to precipitation microphysical characteristics that are related to updraft width and depth, but which also vary due to variable microphysical processes. The effect of microphysical variability on interpretations of convective draft evolution requires further investigation. Instruments place constraints on measurement spatiotemporal coverage, resolution, and accuracy, while models are limited in how accurately they represent the real world. Despite imperfections, ever improving models offer a pathway forward to improve observational strategies to be more targeted and interpretable (e.g., Gettelman et al., 2022). Further research should investigate how well the results shown here apply to other geographical locations and simulations with different setups, using data sets that expand sample sizes beyond those in this study to produce more robust quantification of depth predictors. In addition, more research is needed to quantify updraft shape parameters and the processes that control them given their considerable mediation of conditions and processes that control convective cloud depth. Parameters include not only updraft width and chord lengths but perimeter-to-area ratios, which were not examined here given the relatively coarse 3-km horizontal grid spacing, but which has been shown to correlate with shallow cumulus dilution (e.g., Chen et al., 2023). Exploration of all the above issues has the potential to lead to more accurate predictive models than the regressions used here, particularly for numerous relatively narrow cells, resulting in more accurate quantification of convective cloud depth sensitivities to environmental conditions.

Data Availability Statement

The data sets and code used to generate the analyses shown in this study are available at https://doi.org/10.5281/zenodo.11661885 (Varble, Feng, et al., 2024) including links and information on how to access raw observational data sets and model output.

References

Barth, M. C., Cantrell, C. A., Brune, W. H., Rutledge, S. A., Crawford, J. H., Huntrieser, H., et al. (2015). The deep convective clouds and chemistry (DC3) field campaign. *Bulletin of the American Meteorological Society*, *96*(8), 1281–1309. https://doi.org/10.1175/BAMS-D-13-00290.1

Benjamin, S. G., Brown, J. M., Brunet, G., Lynch, P., Saito, K., & Schlatter, T. W. (2018). 100 years of progress in forecasting and NWP applications. *Meteorological Monographs*, *59*(1), 13-1–13-67. https://doi.org/10.1175/AMSMONOGRAPHS-D-18-0020.1

Acknowledgments
This work was funded by the U.S. Department of Energy's (DOE) Office of Science's Biological and Environmental Research as part of the Atmospheric System Research (ASR) program (ACV, ZF, JNM, AG, JCH, EJ). Additional funding support was provided by NSF Grant AGS-1661662 (ACV, ZZ). Pacific Northwest National Laboratory is operated by Battelle for the DOE under Contract DE-AC05-76RLO1830. Computing support was provided by the National Energy Research Scientific Computing Center, a DOE Office of Science user facility supported by the Office of Science of the U.S. Department of Energy under Contract DE-AC02-05CH11231, as well as the NCAR Computational and Information Systems Laboratory and the University of Utah's Center for High-Performance Computing. The authors thank 3 anonymous reviewers for insightful comments that improved the manuscript.

Blyth, A. M., Cooper, W. A., & Jensen, J. B. (1988). A study of the source of entrained air in Montana Cumuli. *Journal of the Atmospheric Sciences*, *45*(24), 3944–3964. https://doi.org/10.1175/1520-0469(1988)045<3944:ASOTSO>2.0.CO;2

Blyth, A. M., Lasher-Trapp, S. G., & Cooper, W. A. (2005). A study of thermals in cumulus clouds. *Quarterly Journal of the Royal Meteorological Society*, *131*(607), 1171–1190. https://doi.org/10.1256/qj.03.180

Borque, P., Varble, A., & Hardin, J. (2022). Peak rain rate sensitivity to observed cloud condensation nuclei and turbulence in continental warm shallow clouds during CACTI. *Journal of Geophysical Research: Atmospheres*, *127*(16), e2022JD036864. https://doi.org/10.1029/2022JD036864

Brown, R. G., & Zhang, C. (1997). Variability of midtropospheric moisture and its effect on cloud-top height distribution during TOGA COARE. *Journal of the Atmospheric Sciences*, *54*(23), 2760–2774. https://doi.org/10.1175/1520-0469(1997)054<2760:VOMMAI>2.0.CO;2

Bryan, G. H., & Morrison, H. (2012). Sensitivity of a simulated squall line to horizontal resolution and parameterization of microphysics. *Monthly Weather Review*, *140*(1), 202–225. https://doi.org/10.1175/MWR-D-11-00046.1

Bryan, G. H., Wyngaard, J. C., & Fritsch, J. M. (2003). Resolution requirements for the simulation of deep moist convection. *Monthly Weather Review*, *131*(10), 2394–2416. https://doi.org/10.1175/1520-0493(2003)131<2394:RRFTSO>2.0.CO;2

Casanovas, C., Salio, P., Galligani, V., Dolan, B., & Nesbitt, S. W. (2021). Drop size distribution variability in central Argentina during RELAMPAGO-CACTI. *Remote Sensing*, *13*(11), 2026. https://doi.org/10.3390/rs13112026

Chaboureau, J.-P., Guichard, F., Redelsperger, J.-L., & Lafore, J.-P. (2004). The role of stability and moisture in the diurnal cycle of convection over land. *Quarterly Journal of the Royal Meteorological Society*, *130*(604), 3105–3117. https://doi.org/10.1256/qj.03.132

Chen, J., Hagos, S., Xiao, H., Fast, J., Lu, C., Varble, A., et al. (2023). The effects of shallow cumulus cloud shape on interactions among clouds and mixing with near-cloud environments. *Geophysical Research Letters*, *50*(24), e2023GL106334. https://doi.org/10.1029/2023GL106334

Damiani, R., Vali, G., & Haimov, S. (2006). The structure of thermals in cumulus from airborne dual-Doppler radar observations. *Journal of the Atmospheric Sciences*, *63*(5), 1432–1450. https://doi.org/10.1175/JAS3701.1

Derbyshire, S. H., Beau, I., Bechtold, P., Grandpeix, J.-Y., Piriou, J.-M., Redelsperger, J.-L., & Soares, P. M. M. (2004). Sensitivity of moist convection to environmental humidity. *Quarterly Journal of the Royal Meteorological Society*, *130*(604), 3055–3079. https://doi.org/10.1256/qj.03.130

Dessler, A. E., & Sherwood, S. C. (2004). Effect of convection on the summertime extratropical lower stratosphere. *Journal of Geophysical Research*, *109*(D23). https://doi.org/10.1029/2004JD005209

Dickerson, R. R., Huffman, G. J., Luke, W. T., Nunnermacker, L. J., Pickering, K. E., Leslie, A. C. D., et al. (1987). Thunderstorms: An important mechanism in the transport of air pollutants. *Science*, *235*(4787), 460–465. https://doi.org/10.1126/science.235.4787.460

Elkins, C. M., & Hence, D. A. (2024). Radar survey of hail-producing storms and environments during the 2018-2019 severe-weather season in the Córdoba region of Argentina. *Journal of Applied Meteorology and Climatology*, *63*(4), 575–593. https://doi.org/10.1175/JAMC-D-23-0140.1

Fairless, T., & Giangrande, S. (2018). *Interpolated sonde (INTERPOLATEDSONDE)*. ARM User Facility. https://doi.org/10.5439/1095316. accessed 8 March 2021.

Fairless, T., Jensen, M., Zhou, A., & Giangrande, S. E. (2021). *Interpolated Sonde and Gridded Sonde value-added products. ARM Tech. Doc* (p. 7). DOE/SC-ARM-TR-183. Retrieved from https://www.arm.gov/publications/tech_reports/doe-sc-arm-tr-183.pdf

Feng, Z., Hardin, J., Barnes, H. C., Li, J., Leung, L. R., Varble, A., & Zhang, Z. (2023). PyFLEXTRKR: A flexible feature tracking Python software for convective cloud analysis. *Geoscientific Model Development*, *16*(10), 2753–2776. https://doi.org/10.5194/gmd-16-2753-2023

Feng, Z., Varble, A., Hardin, J., Marquis, J., Hunzinger, A., Zhang, Z., & Thieman, M. (2022). Deep convection initiation, growth, and environments in the complex terrain of central Argentina during CACTI. *Monthly Weather Review*, *150*(5), 1135–1155. https://doi.org/10.1175/MWR-D-21-0237.1

Gaustad, K. L., Turner, D. D., & McFarlane, S. A. (2011). *MWRRET value-added product: The retrieval of liquid water path and precipitable water vapor from microwave radiometer (MWR) data sets* (p. 5). ARM Tech. Doc. DOE/SC-ARM/TR-081.2. Retrieved from https://www.arm.gov/publications/tech_reports/doe-sc-arm-tr-081.2.pdf

Gettelman, A., Geer, A. J., Forbes, R. M., Carmichael, G. R., Feingold, G., Posselt, D. J., et al. (2022). The future of Earth system prediction: Advances in model-data fusion. *Science Advances*, *8*(14), eabn3488. https://doi.org/10.1126/sciadv.abn3488

Giangrande, S. E., Biscaro, T. S., & Peters, J. M. (2023). Seasonal controls on isolated convective storm drafts, precipitation intensity, and life cycle as observed during GoAmazon2014/5. *Atmospheric Chemistry and Physics*, *23*(9), 5297–5316. https://doi.org/10.5194/acp-23-5297-2023

Ginoux, P., Chin, M., Tegen, I., Prospero, J. M., Holben, B., Dubovik, O., & Lin, S.-J. (2001). Sources and distributions of dust aerosols simulated with the GOCART model. *Journal of Geophysical Research*, *106*(D17), 20255–20273. https://doi.org/10.1029/2000JD000053

Grabowski, W. W., Bechtold, P., Cheng, A., Forbes, R., Halliwell, C., Khairoutdinov, M., et al. (2006). Daytime convective development over land: A model intercomparison based on LBA observations. *Quarterly Journal of the Royal Meteorological Society*, *132*(615), 317–344. https://doi.org/10.1256/qj.04.147

Hannah, W. M. (2017). Entrainment versus dilution in tropical deep convection. *Journal of the Atmospheric Sciences*, *74*(11), 3725–3747. https://doi.org/10.1175/JAS-D-16-0169.1

Hardin, J., Bharadwaj, N., Giangrande, S. E., Varble, A., & Feng, Z. (2020). Taranis: A new framework for physically constrained radar processing. In *2020 fall meeting, online, American Geophysical Union, Abstract A159-08*. Retrieved from https://agu.confex.com/agu/fm20/meetingapp.cgi/Paper/699052

Hardin, J., Bharadwaj, N., Varble, A., Giangrande, S., & Feng, Z. (2024). PI data: CACTI CSAPR2 Taranis retrievals. https://doi.org/10.5439/2440152

Hardin, J., Hunzinger, A., Schuman, E., Matthews, A., Bharadwaj, N., Varble, A., et al. (2018). *C-band scanning ARM precipitation radar, CF-radial, quality-controlled plan position indicator scans (CSAPR2CFRPPIQC)*. ARM User Facility. https://doi.org/10.5439/1615604. accessed 9 March 2021.

Hardin, J., Hunzinger, A., Schuman, E., Matthews, A., Bharadwaj, N., Varble, A., et al. (2020). *CACTI radar b1 processing: Corrections, calibrations, and processing report* (p. 46). ARM Tech. Doc. DOE/SC-ARM-TR-244. Retrieved from https://arm.gov/publications/brochures/doe-sc-arm-tr-244.pdf

Helmus, J. J., & Collis, S. M. (2016). The python ARM radar toolkit (Py-ART), a library for working with weather radar data in the python programming language. *Journal of Open Research Software*, *4*(1), e25. https://doi.org/10.5334/jors.119

Hernandez-Deckers, D., & Sherwood, S. C. (2016). A numerical investigation of cumulus thermals. *Journal of the Atmospheric Sciences*, *73*(10), 4117–4136. https://doi.org/10.1175/JAS-D-15-0385.1

Hersbach, H., Bell, B., Berrisford, P., Hirahara, S., Horányi, A., Muñoz-Sabater, J., et al. (2020). The ERA5 global reanalysis. *Quarterly Journal of the Royal Meteorological Society*, *146*(730), 1999–2049. https://doi.org/10.1002/qj.3803

Houston, A. L., & Niyogi, D. (2007). The sensitivity of convective initiation to the lapse rate of the active cloud-bearing layer. *Monthly Weather Review*, *135*(9), 3013–3032. https://doi.org/10.1175/MWR3449.1

Houze, R. A., Jr. (1973). A climatological study of vertical transports by cumulus-scale convection. *Journal of the Atmospheric Sciences*, *30*(6), 1112–1123. https://doi.org/10.1175/1520-0469(1973)030<1112:ACSOVT>2.0.CO;2

Iacono, M. J., Delamere, J. S., Mlawer, E. J., Shephard, M. W., Clough, S. A., & Collins, W. D. (2008). Radiative forcing by long-lived greenhouse gases: Calculations with the AER radiative transfer models. *Journal of Geophysical Research*, *113*(D13), D13103. https://doi.org/10.1029/2008JD009944

Igel, A. L., & van den Heever, S. C. (2021). Invigoration or enervation of convective clouds by aerosols? *Geophysical Research Letters*, *48*(16), e2021GL093804. https://doi.org/10.1029/2021GL093804

Igel, M. R., & van den Heever, S. C. (2015). The relative influence of environmental characteristics on tropical deep convective morphology as observed by CloudSat. *Journal of Geophysical Research: Atmospheres*, *120*(9), 4304–4322. https://doi.org/10.1002/2014JD022690

Janjić, Z. I. (1994). The step-mountain eta coordinate model: Further developments of the convection, viscous sublayer, and turbulence closure schemes. *Monthly Weather Review*, *122*(5), 927–945. https://doi.org/10.1175/1520-0493(1994)122<0927:TSMECM>2.0.CO;2

Khairoutdinov, M., & Randall, D. (2006). High-resolution simulation of shallow-to-deep convection transition over land. *Journal of the Atmospheric Sciences*, *63*(12), 3421–3436. https://doi.org/10.1175/JAS3810.1

Kirshbaum, D. J. (2011). Cloud-resolving simulations of deep convection over a heated mountain. *Journal of the Atmospheric Sciences*, *68*(2), 361–378. https://doi.org/10.1175/2010JAS3642.1

Kirshbaum, D. J. (2013). On thermally forced circulations over heated terrain. *Journal of the Atmospheric Sciences*, *70*(6), 1690–1709. https://doi.org/10.1175/JAS-D-12-0199.1

Kirshbaum, D. J., & Straub, D. N. (2019). Linear theory of shallow convection in deep, vertically sheared atmospheres. *Quarterly Journal of the Royal Meteorological Society*, *145*(724), 3129–3147. https://doi.org/10.1002/qj.3609

Kuang, Z., & Bretherton, C. S. (2006). A mass-flux scheme view of a high-resolution simulation of a transition from shallow to deep cumulus convection. *Journal of the Atmospheric Sciences*, *63*(7), 1895–1909. https://doi.org/10.1175/JAS3723.1

Lang, T. J., Ávila, E. E., Blakeslee, R. J., Burchfield, J., Wingo, M., Bitzer, P. M., et al. (2020). The RELAMPAGO lightning mapping array: Overview and initial comparison with the geostationary lightning mapper. *Journal of Atmospheric and Oceanic Technology*, *37*(8), 1457–1475. https://doi.org/10.1175/JTECH-D-20-0005.1

Lareau, N. P., Knopp, T., & Kirshbaum, D. J. (2024). Mechanical and thermal forcing for upslope flows and cumulus convection over the Sierras de Córdoba. *Monthly Weather Review*, *152*(9), 2149–2167. https://doi.org/10.1175/MWR-D-23-0254.1

LeBel, L. J., & Markowski, P. M. (2023). An analysis of the impact of vertical wind shear on convection initiation using large-eddy simulations: Importance of wake entrainment. *Monthly Weather Review*, *151*(7), 1667–1688. https://doi.org/10.1175/MWR-D-22-0176.1

Lebo, Z. J., & Morrison, H. (2015). Effects of horizontal and vertical grid spacing on mixing in simulated squall lines and implications for convective strength and structure. *Monthly Weather Review*, *143*(11), 4355–4375. https://doi.org/10.1175/MWR-D-15-0154.1

LeMone, M. A. (1983). Momentum transport by a line of cumulonimbus. *Journal of the Atmospheric Sciences*, *40*(7), 1815–1834. https://doi.org/10.1175/1520-0469(1983)040<1815:MTBALO>2.0.CO;2

Lindeman, R. H., Merenda, P. F., & Gold, R. Z. (1980). Introduction to bivariate and multivariate analysis. *Glenview, IL: Scott Foresman and Company*.

Liu, S., Sindhu, K. D., & Kirshbaum, D. J. (2023). Observations of boundary layer convergence lines and associated updrafts in the U.S. Southern Great Plains. *Journal of the Atmospheric Sciences*, *80*(12), 2947–2968. https://doi.org/10.1175/JAS-D-23-0089.1

Lock, N. A., & Houston, A. L. (2014). Empirical examination of the factors regulating thunderstorm initiation. *Monthly Weather Review*, *142*(1), 240–258. https://doi.org/10.1175/MWR-D-13-00082.1

Lombardo, K., & Kumjian, M. R. (2022). Observations of the discrete propagation of a mesoscale convective system during RELAMPAGO–CACTI. *Monthly Weather Review*, *150*(8), 2111–2138. https://doi.org/10.1175/MWR-D-21-0265.1

Louf, V., Jakob, C., Protat, A., Bergemann, M., & Narsey, S. (2019). The relationship of cloud number and size with their large-scale environment in deep tropical convection. *Geophysical Research Letters*, *46*(15), 9203–9212. https://doi.org/10.1029/2019GL083964

Lucas, C., Zipser, E. J., & Lemone, M. A. (1994). Vertical velocity in oceanic convection off tropical Australia. *Journal of the Atmospheric Sciences*, *51*(21), 3183–3193. https://doi.org/10.1175/1520-0469(1994)051<3183:VVIOCO>2.0.CO;2

Mapes, B., & Houze, R. A., Jr. (1992). An integrated view of the 1987 Australian monsoon and its mesoscale convective systems. I: Horizontal structure. *Quarterly Journal of the Royal Meteorological Society*, *118*(507), 927–963. https://doi.org/10.1002/qj.49711850706

Markowski, P., Hannon, C., & Rasmussen, E. (2006). Observations of convection initiation "failure" from the 12 June 2002 IHOP deployment. *Monthly Weather Review*, *134*(1), 375–405. https://doi.org/10.1175/MWR3059.1

Marquis, J. N., Feng, Z., Varble, A., Nelson, T. C., Houston, A., Peters, J. M., et al. (2023). Near-cloud atmospheric ingredients for deep convection initiation. *Monthly Weather Review*, *151*(5), 1247–1267. https://doi.org/10.1175/MWR-D-22-0243.1

Marquis, J. N., Varble, A. C., Robinson, P., Nelson, T. C., & Friedrich, K. (2021). Low-level mesoscale and cloud-scale interactions promoting deep convection initiation. *Monthly Weather Review*, *149*(8), 2473–2495. https://doi.org/10.1175/MWR-D-20-0391.1

Medina, B. L., Carey, L. D., Bitzer, P. M., Lang, T. J., & Deierling, W. (2022). The Relation of environmental conditions with charge structure in central Argentina thunderstorms. *Earth and Space Science*, *9*(5), e2021EA002193. https://doi.org/10.1029/2021EA002193

Medina, B. L., Carey, L. D., Deierling, W., & Lang, T. (2022). Microphysical and kinematic characteristics of anomalous charge structure thunderstorms in Cordoba, Argentina. *Atmosphere*, *13*(8), 1329. https://doi.org/10.3390/atmos13081329

Minnis, P., Sun-Mack, S., Chen, Y., Chang, F.-L., Yost, C. R., Smith, W. L., Jr., et al. (2021). CERES MODIS cloud product retrievals for edition 4—Part I: Algorithm changes. *IEEE Transactions on Geoscience and Remote Sensing*, *59*(4), 2744–2780. https://doi.org/10.1109/TGRS.2020.3008866

Moncrieff, M. W. (1992). Organized convective systems: Archetypal dynamical models, mass and momentum flux theory, and parametrization. *Quarterly Journal of the Royal Meteorological Society*, *118*(507), 819–850. https://doi.org/10.1002/qj.49711850703

Monin, A. S., & Obukhov, A. M. (1954). Basic laws of turbulent mixing in the surface layer of the atmosphere. *Contrib. Geophys. Inst. Acad. Sci. USSR*, *151*, 163–187.

Morrison, H. (2017). An analytic description of the structure and evolution of growing deep cumulus updrafts. *Journal of the Atmospheric Sciences*, *74*(3), 809–834. https://doi.org/10.1175/JAS-D-16-0234.1

Morrison, H., Peters, J. M., Chandrakar, K. K., & Sherwood, S. C. (2022). Influences of environmental relative humidity and horizontal scale of subcloud ascent on deep convective initiation. *Journal of the Atmospheric Sciences*, *79*(2), 337–359. https://doi.org/10.1175/JAS-D-21-0056.1

Morrison, H., Peters, J. M., Varble, A. C., Hannah, W. M., & Giangrande, S. E. (2020). Thermal chains and entrainment in cumulus updrafts. Part I: Theoretical description. *Journal of the Atmospheric Sciences*, *77*(11), 3637–3660. https://doi.org/10.1175/JAS-D-19-0243.1

Moser, D. H., & Lasher-Trapp, S. (2017). The influence of successive thermals on entrainment and dilution in a simulated cumulus congestus. *Journal of the Atmospheric Sciences*, *74*(2), 375–392. https://doi.org/10.1175/JAS-D-16-0144.1

Mulholland, J. P., Nesbitt, S. W., Trapp, R. J., & Peters, J. M. (2020). The influence of terrain on the convective environment and associated convective morphology from an idealized modeling perspective. *Journal of the Atmospheric Sciences*, *77*(11), 3929–3949. https://doi.org/10.1175/JAS-D-19-0190.1

Mulholland, J. P., Nesbitt, S. W., Trapp, R. J., Rasmussen, K. L., & Salio, P. V. (2018). Convective storm life cycle and environments near the Sierras de Córdoba, Argentina. *Monthly Weather Review*, *146*(8), 2541–2557. https://doi.org/10.1175/MWR-D-18-0081.1

Mulholland, J. P., Peters, J. M., & Morrison, H. (2021). How does LCL height influence deep convective updraft width? *Geophysical Research Letters*, *48*(13), e2021GL093316. https://doi.org/10.1029/2021GL093316

Mullendore, G. L., Homann, A. J., Jorgenson, S. T., Lang, T. J., & Tessendorf, S. A. (2013). Relationship between level of neutral buoyancy and dual-Doppler observed mass detrainment levels in deep convection. *Atmospheric Chemistry and Physics*, *13*(1), 181–190. https://doi.org/10.5194/acp-13-181-2013

Nakanishi, M., & Niino, H. (2006). An improved Mellor–Yamada level-3 model: Its numerical stability and application to a regional prediction of advection fog. *Boundary-Layer Meteorology*, *119*(2), 397–407. https://doi.org/10.1007/s10546-005-9030-8

Nakanishi, M., & Niino, H. (2009). Development of an improved turbulence closure model for the atmospheric boundary layer. *Journal of the Meteorological Society of Japan*, *87*(5), 895–912. https://doi.org/10.2151/jmsj.87.895

Nelson, T. C., Marquis, J., Peters, J. M., & Friedrich, K. (2022). Environmental controls on simulated deep moist convection initiation occurring during RELAMPAGO-CACTI. *Journal of the Atmospheric Sciences*, *79*(7), 1941–1964. https://doi.org/10.1175/JAS-D-21-0226.1

Nelson, T. C., Marquis, J., Varble, A., & Friedrich, K. (2021). Radiosonde observations of environments supporting deep moist convection initiation during RELAMPAGO-CACTI. *Monthly Weather Review*, *149*(1), 289–309. https://doi.org/10.1175/MWR-D-20-0148.1

Nesbitt, S. W., Salio, P. V., Ávila, E., Bitzer, P., Carey, L., Chandrasekar, V., et al. (2021). A storm safari in subtropical South America: Proyecto RELAMPAGO. *Bulletin of the American Meteorological Society*, *102*(8), E1621–E1644. https://doi.org/10.1175/BAMS-D-20-0029.1

Pan, L. L., Honomichi, S. B., Kinnison, D. E., Abalos, M., Randel, W. J., Bergman, J. W., & Bian, J. (2014). Transport of chemical tracers from the boundary layer to stratosphere associated with the dynamics of the Asian summer monsoon. *Journal of Geophysical Research: Atmospheres*, *121*(24), 14159–14174. https://doi.org/10.1002/2016JD025616

Pedregosa, F., Varoquaux, G., Gramfort, A., Michel, V., Thirion, B., Grisel, O., et al. (2011). Scikit-learn: Machine learning in python. *Journal of Machine Learning Research*, *12*, 2825–2830.

Peters, J. M., Hannah, W., & Morrison, H. (2019). The influence of vertical wind shear on moist thermals. *Journal of the Atmospheric Sciences*, *76*(6), 1645–1659. https://doi.org/10.1175/JAS-D-18-0296.1

Peters, J. M., Lebo, Z. J., Chavas, D. R., & Su, C.-Y. (2023). Entrainment makes pollution more likely to weaken deep convective updrafts than invigorate them. *Geophysical Research Letters*, *50*(12), e2023GL103314. https://doi.org/10.1029/2023GL103314

Peters, J. M., Morrison, H., Nelson, T. C., Marquis, J. N., Mulholland, J. P., & Nowotarski, C. J. (2022a). The influence of shear on deep convection initiation. Part I: Theory. *Journal of the Atmospheric Sciences*, *79*(6), 1669–1690. https://doi.org/10.1175/JAS-D-21-0145.1

Peters, J. M., Morrison, H., Nelson, T. C., Marquis, J. N., Mulholland, J. P., & Nowotarski, C. J. (2022b). The influence of shear on deep convection initiation. Part II: Simulations. *Journal of the Atmospheric Sciences*, *79*(6), 1691–1711. https://doi.org/10.1175/JAS-D-21-0144.1

Peters, J. M., Morrison, H., Varble, A. C., Hannah, W. M., & Giangrande, S. E. (2020). Thermal chains and entrainment in cumulus updrafts. Part II: Analysis of idealized simulations. *Journal of the Atmospheric Sciences*, *77*(11), 3661–3681. https://doi.org/10.1175/JAS-D-19-0244.1

Powell, S. W. (2024). Updraft width implications for cumulonimbus growth in a moist marine environment. *Journal of the Atmospheric Sciences*, *81*(3), 629–648. https://doi.org/10.1175/JAS-D-23-0065.1

Prein, A. F., Rasmussen, R. M., Wang, D., & Giangrande, S. E. (2021). Sensitivity of organized convective storms to model grid spacing in current and future climates. *Philosophical Transactions of the Royal Society A*, *379*(2195), 20190546. https://doi.org/10.1098/rsta.2019.0546

Rasmussen, K. L., & Houze, R. A., Jr. (2011). Orogenic convection in subtropical South America as seen by the TRMM satellite. *Monthly Weather Review*, *139*(8), 2399–2420. https://doi.org/10.1175/MWR-D-10-05006.1

Rasmussen, K. L., & Houze, R. A., Jr. (2016). Convective initiation near the Andes in subtropical South America. *Monthly Weather Review*, *144*(6), 2351–2374. https://doi.org/10.1175/MWR-D-15-0058.1

Riehl, H., & Malkus, J. (1958). On the heat balance of the equatorial trough zone. *Geophysica*, *6*, 503–538.

Rivelli Zea, L., Nesbitt, S. W., Ladino, A., Hardin, J. C., & Varble, A. (2021). Raindrop size spectrum in deep convective regions of the Americas. *Atmosphere*, *12*(8), 979. https://doi.org/10.3390/atmos12080979

Rocque, M. N., Deierling, W., Rasmussen, K. L., Albrecht, R. I., & Medina, B. L. (2024). Lightning characteristics associated with storm modes observed during RELAMPAGO. *Journal of Geophysical Research: Atmospheres*, *129*(4), e2023JD039520. https://doi.org/10.1029/2023JD03952

Romps, D. M., & Charn, A. B. (2015). Sticky thermals: Evidence for a dominant balance between buoyancy and drag in cloud updrafts. *Journal of the Atmospheric Sciences*, *72*(8), 2890–2901. https://doi.org/10.1175/JAS-D-15-0042.1

Ross, T. I. D., & Lasher-Trapp, S. (2024). On CCN effects upon convective cold pool timing and features. *Monthly Weather Review*, *152*(3), 891–906. https://doi.org/10.1175/MWR-D-23-0154.1

Rousseau-Rizzi, R., Kirshbaum, D. J., & Yau, M. K. (2017). Initiation of deep convection over an idealized mesoscale convergence line. *Journal of the Atmospheric Sciences*, *74*(3), 835–853. https://doi.org/10.1175/JAS-D-16-0221.1

Sasaki, C. R. S., Rowe, A. K., McMurdie, L. A., Varble, A. C., & Zhang, Z. (2024). Influences of the South American low-level jet on the convective environment in Central Argentina using a convection-permitting simulation. *Monthly Weather Review*, *152*(2), 629–648. https://doi.org/10.1175/MWR-D-23-0122.1

Schlemmer, L., & Hohenegger, C. (2014). The formation of wider and deeper clouds as a result of cold-pool dynamics. *Journal of the Atmospheric Sciences*, *71*(8), 2842–2858. https://doi.org/10.1175/JAS-D-13-0170.1

Schumacher, R. S., Hence, D. A., Nesbitt, S. W., Trapp, R. J., Kosiba, K. A., Wurman, J., et al. (2021). Convective-storm environments in subtropical South America from high-frequency soundings during RELAMPAGO-CACTI. *Monthly Weather Review*, *149*(5), 1439–1458. https://doi.org/10.1175/MWR-D-20-0293.1

Sherwood, S. C. (1999). Convective precursors and predictability in the tropical Western Pacific. *Monthly Weather Review*, *127*(12), 2977–2991. https://doi.org/10.1175/1520-0493(1999)127<2977:CPAPIT>2.0.CO;2

Sherwood, S. C., Hernández-Deckers, D., Colin, M., & Robinson, F. (2013). Slippery thermals and the cumulus entrainment paradox. *Journal of the Atmospheric Sciences*, *70*(8), 2426–2442. https://doi.org/10.1175/JAS-D-12-0220.1

Singh, I., Nesbitt, S. W., & Davis, C. A. (2022). Quasi-idealized numerical simulations of processes involved in orogenic convection initiation over the Sierras de Córdoba. *Journal of the Atmospheric Sciences*, *79*(4), 1127–1149. https://doi.org/10.1175/JAS-D-21-0007.1

Skamarock, W. C., Klemp, J. B., Dudhia, J., Gill, D. O., Liu, Z., Berner, J., et al. (2019). *A description of the advanced research WRF model version 4* (p. 145). NCAR Tech. Note NCAR/TN-556+STR. https://doi.org/10.5065/1dfh-6p97

Smith, P. L. (1984). Equivalent radar reflectivity factors for snow and ice particles. *Journal of Climate and Applied Meteorology*, *23*(8), 1258–1260. https://doi.org/10.1175/1520-0450(1984)023<1258:ERRFFS>2.0.CO;2

Smith, W. L., & Thieman, M. (2019). *Minnis cloud products using VISST algorithm (VISSTPX2DRECTG16V4MINNIS)*. ARM User Facility. Retrieved from https://adc.arm.gov/discovery/#/results/s::corvisstpx2drectg16v4minnisX1.c1. accessed 26 February 2021.

Steiner, M., Houze, R. A., Jr., & Yuter, S. E. (1995). Climatological characterization of three-dimensional storm structure from operational radar and rain Gauge data. *Journal of Applied Meteorology and Climatology*, *34*(9), 1978–2007. https://doi.org/10.1175/1520-0450(1995)034<1978:CCOTDS>2.0.CO;2

Stevens, B., Satoh, M., Auger, L., Biercamp, J., Bretherton, C. S., Chen, X., et al. (2019). DYAMOND: The DYnamics of the Atmospheric general circulation Modeled On Non-hydrostatic Domains. *Progress in Earth and Planetary Science*, *6*(1), 61. https://doi.org/10.1186/s40645-019-0304-z

Takahashi, H., & Luo, Z. (2012). Where is the level of neutral buoyancy for deep convection? *Geophysical Research Letters*, *39*(15), L15809. https://doi.org/10.1029/2012GL052638

Takahashi, H., Luo, Z. J., & Stephens, G. (2021). Revisiting the entrainment relationship of convective plumes: A perspective from global observations. *Geophysical Research Letters*, *48*(6), e2020GL092349. https://doi.org/10.1029/2020GL092349

Takahashi, H., Luo, Z. J., Stephens, G., & Mulholland, J. P. (2023). Revisiting the land-ocean contrasts in deep convective cloud intensity using global satellite observations. *Geophysical Research Letters*, *50*(5), e2022GL102089. https://doi.org/10.1029/2022GL102089

Takemi, T., Hirayama, O., & Liu, C. (2004). Factors responsible for the vertical development of tropical oceanic cumulus convection. *Geophysical Research Letters*, *31*(11), L11109. https://doi.org/10.1029/2004GL020225

Tang, S. L., & Kirshbaum, D. J. (2020). On the sensitivity of deep-convection initiation to horizontal grid resolution. *Quarterly Journal of the Royal Meteorological Society*, *146*(728), 1085–1105. https://doi.org/10.1002/qj.3726

Tewari, M., Chen, F., Wang, W., Dudhia, J., LeMone, M. A., Mitchell, K., et al. (2004). Implementation and verification of the unified NOAH land surface model in the WRF model. In *20th conference on weather analysis and forecasting/16th conference on numerical weather prediction*. American Meteorological Society, Abstract 14.2a. Retrieved from https://ams.confex.com/ams/84Annual/techprogram/paper_69061.htm

Thompson, G., & Eidhammer, T. (2014). A study of aerosol impacts on clouds and precipitation development in a large winter cyclone. *Journal of the Atmospheric Sciences*, *71*(10), 3636–3658. https://doi.org/10.1175/JAS-D-13-0305.1

Tian, Y., Zhang, Y., Klein, S. A., & Schumacher, C. (2021). Interpreting the diurnal cycle of clouds and precipitation in the ARM GoAmazon observations: Shallow to deep convection transition. *Journal of Geophysical Research: Atmospheres*, *126*(5), e2020JD033766. https://doi.org/10.1029/2020JD033766

Trapp, R. J., Kosiba, K. A., Marquis, J. N., Kumjian, M. R., Nesbitt, S. W., Wurman, J., et al. (2020). Multiple-platform and multiple-Doppler Radar observations of a supercell thunderstorm in South America during RELAMPAGO. *Monthly Weather Review*, *148*(8), 3225–3241. https://doi.org/10.1175/MWR-D-20-0125.1

Trepte, Q. Z., Minnis, P., Sun-Mack, S., Yost, C. R., Chen, Y., Jin, Z., et al. (2019). Global cloud detection for CERES edition 4 using Terra and Aqua MODIS data. *IEEE Transactions on Geoscience and Remote Sensing*, *57*(11), 9410–9449. https://doi.org/10.1109/TGRS.2019.2926620

Turner, D. D., Clough, S. A., Liljegren, J. C., Clouthiaux, E. E., Cady-Pereira, K., & Gaustad, K. L. (2007). Retrieving liquid water path and precipitable water vapor from the Atmospheric Radiation Measurement (ARM) microwave radiometers. *IEEE Transactions on Geoscience and Remote Sensing*, *45*(11), 3680–3689. https://doi.org/10.1109/TGRS.2007.903703

Varble, A., Feng, Z., Marquis, J. N., Zhang, Z., Geiss, A., Hardin, J. C., & Jo, E. (2024). Data and Code for "Updraft Width Modulates Ambient Atmospheric Controls on Convective Cloud Depth" by Varble et al. (2024) [Dataset]. In *Journal of Geophysical Research: Atmospheres Zenodo*. https://doi.org/10.5281/zenodo.11661885

Varble, A., Morrison, H., & Zipser, E. (2020). Effects of under-resolved convective dynamics on the evolution of a squall line. *Monthly Weather Review*, *148*(1), 289–311. https://doi.org/10.1175/MWR-D-19-0187.1

Varble, A., Thieman, M., Spangenberg, D., Bedka, K., Smith, W., Jr., & Hardin, J. (2024). PI data: Parallax-corrected VISST-derived pixel-level products from satellite GOES-16. https://doi.org/10.5439/2008448

Varble, A., Zipser, E. J., Fridlind, A. M., Zhu, P., Ackerman, A. S., Chaboureau, J.-P., et al. (2014). Evaluation of cloud-resolving and limited area model intercomparison simulations using TWP-ICE observations: 1. Deep convective updraft properties. *Journal of Geophysical Research: Atmospheres*, *119*(24), 13891–13918. https://doi.org/10.1002/2013JD021371

Varble, A. C., Igel, A. L., Morrison, H., Grabowski, W. W., & Lebo, Z. J. (2023). Opinion: A critical evaluation of the evidence for aerosol invigoration of deep convection. *Atmospheric Chemistry and Physics*, *23*(21), 13791–13808. https://doi.org/10.5194/acp-23-13791-2023

Varble, A. C., Nesbitt, S. W., Salio, P., Hardin, J. C., Bharadwaj, N., Borque, P., et al. (2021). Utilizing a storm-generating hotspot to study convective cloud transitions: The CACTI experiment. *Bulletin of the American Meteorological Society*, *102*(8), E1597–E1620. https://doi.org/10.1175/BAMS-D-20-0030.1

Veals, P. G., Varble, A. C., Russell, J. O. H., Hardin, J. C., & Zipser, E. J. (2022). Indications of a decrease in the depth of deep convective cores with increasing aerosol concentration during the CACTI campaign. *Journal of the Atmospheric Sciences*, *79*(3), 705–722. https://doi.org/10.1175/JAS-D-21-0119.1

Wang, D., Giangrande, S. E., Feng, Z., Hardin, J. C., & Prein, A. F. (2020). Updraft and downdraft core size and intensity as revealed by radar wind profilers: MCS observations and idealized model comparisons. *Journal of Geophysical Research: Atmospheres*, *125*(11), e2019JD031774. https://doi.org/10.1029/2019JD031774

Wang, D., Jensen, M. P., D'Iorio, J. A., Jozef, G., Giangrande, S. E., Johnson, K. L., et al. (2020). An observational comparison of level of neutral buoyancy and level of maximum detrainment in tropical deep convective clouds. *Journal of Geophysical Research: Atmospheres*, *125*(16), e2020JD032637. https://doi.org/10.1029/2020JD032637

Wang, P. K. (2003). Moisture plumes above thunderstorm anvils and their contributions to cross-tropopause transport of water vapor in mid-latitudes. *Journal of Geophysical Research*, *108*(D6), 4194. https://doi.org/10.1029/2002JD002581

Wu, C., Stevens, B., & Arakawa, A. (2009). What controls the transition from shallow to deep convection? *Journal of the Atmospheric Sciences*, *66*(6), 1793–1806. https://doi.org/10.1175/2008JAS2945.1

Yang, G., & Slingo, J. (2001). The diurnal cycle in the tropics. *Monthly Weather Review*, *129*(4), 784–801. https://doi.org/10.1175/1520-0493(2001)129<0784:TDCITT>2.0.CO;2

Yost, C. R., Minnis, P., Sun-Mack, S., Chen, Y., & Smith, W. L. (2021). CERES MODIS cloud product retrievals for edition 4—Part II: Comparisons to CloudSat and CALIPSO. *IEEE Transactions on Geoscience and Remote Sensing*, *59*(5), 3695–3724. https://doi.org/10.1109/TGRS.2020.3015155

Zhang, Y., & Klein, S. A. (2010). Mechanisms affecting the transition from shallow to deep convection over land: Inferences from observations of the diurnal cycle collected at the ARM Southern Great Plains Site. *Journal of the Atmospheric Sciences*, *67*(9), 2943–2959. https://doi.org/10.1175/2010JAS3366.1

Zhang, Z., Varble, A., Feng, Z., Hardin, J., & Zipser, E. (2021). Growth of mesoscale convective systems in observations and a seasonal convection-permitting simulation over Argentina. *Monthly Weather Review*, *149*(10), 3469–3490. https://doi.org/10.1175/MWR-D-20-0411.1

Zhang, Z., Varble, A. C., Feng, Z., Marquis, J., Hardin, J. C., & Zipser, E. J. (2024). Dependencies of simulated convective cell and system growth biases on atmospheric instability and model resolution. *Journal of Geophysical Research: Atmospheres, 129*(22), e2024JD04190. https://doi.org/10.1029/2024JD041090

Zhao, M., & Austin, P. H. (2005). Life cycle of numerically simulated shallow cumulus clouds. Part II: Mixing dynamics. *Journal of the Atmospheric Sciences*, *62*(5), 1291–1310. https://doi.org/10.1175/JAS3415.1

Zhuang, J. (2020). *xESMF: Universal regridder for geospatial data*. Zenodo. https://doi.org/10.5281/zenodo.3700105

Zipser, E. J. (2003). Some views on "hot towers" after 50 years of tropical field programs and two years of TRMM data. *Meteorological Monographs*, *29*(51), 49–58. https://doi.org/10.1175/0065-9401(2003)029<0049:CSVOHT>2.0.CO;2